EVALUATION OF ASTER SATELLITE DATA FOR GEOLOGICAL APPLICATIONS

Consultancy Report to Geoscience Australia

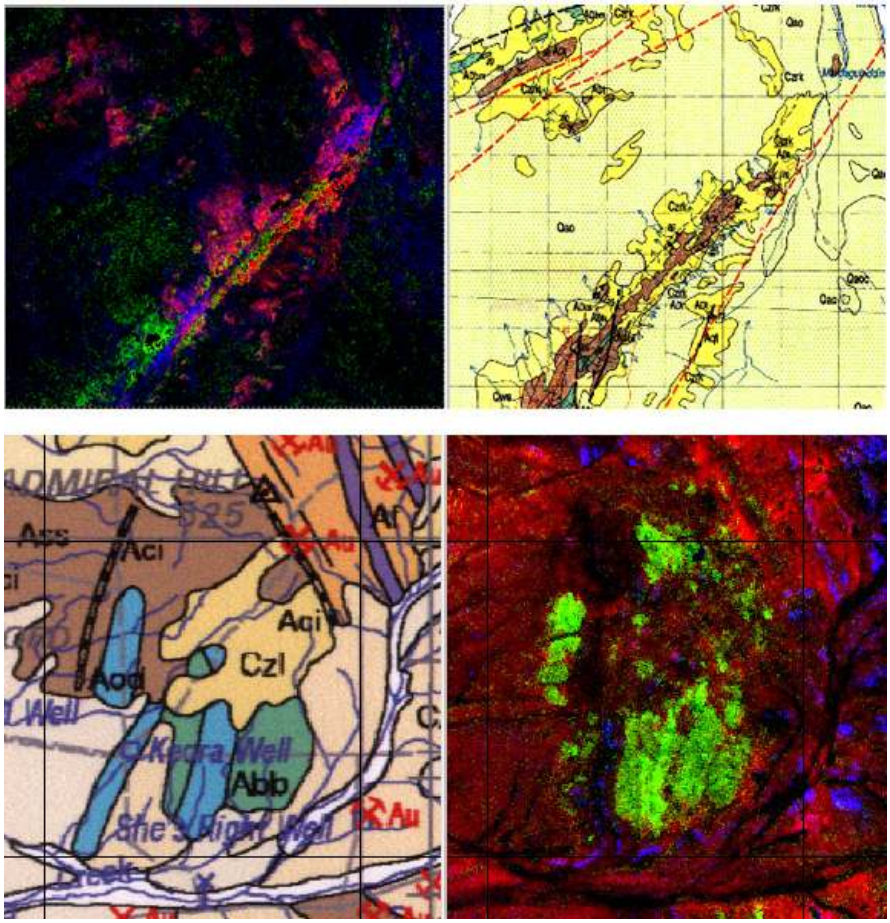

By P. N. Bierwirth

6 May 2002

0.0 Summary

The ASTER satellite sensor, at medium spectral resolution, poses a challenge for the analyst. It is clear that there is a need for demonstrated examples of ASTER analysis. Currently the user is confronted, not only with unfamiliar data, but also with a confusing array of potential methodologies and software, many of them involving an expert knowledge in remote sensing. The aim of this project was to investigate the available methods of ASTER analysis for areas that have known mineral distributions. At Indee, (Pilbara, W.A), ASTER analysis results are compared with airborne hyperspectral data and field data. The second area, Laverton, W.A., is the subject of a recent map release (Stewart, 2001).

In general, the ASTER data quality is good and registration between bands appears adequate for analysis. Comparisons with Landsat TM shows that ASTER has much improved spatial resolution in the VNIR and far greater spectral resolution in the SWIR.

The level 2 (AST_07) reflectance product has some significant problems both for use in visual identification of spectral features and for analysis of end-members. This was evident in (1) band 9 reflectance being nearly twice as high as expected and (2) the presence of an unrealistic 2.165 μm absorption feature in pixels with high SWIR reflectance. These problems can be overcome by performing a gain and offset correction to the ASTER level 1B radiance data. It was found in this work that the analysis of corrected level 1B data provided slightly better results than level 2 reflectance data.

For the Indee, Pilbara, case study area, ASTER analysis was partially successful in mapping carbonate, Fe-chlorite, white-mica, kaolinite, tourmaline, talc and Fe-oxides. The analysis did not work for pyrophyllite. For the partially successful minerals, there were problems due to mixing and spectral similarity between end-members. Dolomite and calcite separation was not achieved, Fe-chlorite was not detected when mixed with kaolinite and white mica and kaolinite images were partially mixed.

In the Laverton area, ASTER rock-type end-members shows the subtle change in rock units between acid, intermediate to basic igneous units, information that is not represented on the geological map. An amphibole end-member image was very successful at mapping mafic rock exposures, identifying grossly incorrect mapping in the 2nd edition mapping that was actually correct in the 1st edition map. ASTER laterite mapping has implications for Nickel exploration in the region.

In general, Mixture Tuned Matched Filtering (MTMF) produced best results for mapping mineral concentrations. Non-unmixing methods such as Spectral Angle Mapper (SAM) and ratios are prone to effects due to mixing, particularly those due to vegetation.

The ASTER level 2 thermal emissivity (TES) data appears to be successful at removing temperature effects from the spectral data. Thermal IR data were found to be valuable, particularly in the Laverton area, for mapping quartz rich units and the

dispersion of associated sandy soils. Basic units are sometimes observable in the thermal data, but are often difficult to discern from vegetation, which clearly has a masking effect.

The presence of accurate ground mineral concentration information is an advantage for image analysis. The presence of hyperspectral mineral maps at Indee appears to have resulted in a much more definitive result in terms of individual minerals compared with the Laverton area. It is recommended that ASTER analysis be accompanied by a localized airborne hyperspectral survey or at least ground-based spectral measurements.

In conclusion, it is clear that ASTER represents a scientific advance on Landsat TM data. It has the clear capability of mapping multiple geological components that are often difficult to map on the ground. Given its availability at low cost, this system should be widely employed in geological studies.

Table of Contents

1.0 Introduction

1.1 The ASTER sensor

The Advanced Spaceborne Thermal Emission and Reflection Radiometer (ASTER) sensor is carried by the Terra satellite, which was launched on December 18, 1999 with a planned operation period of 6 years. It operates on a sun-synchronous orbit with a complete recurrence of 16 days (returning to it's starting orbit). Importantly, it flies about 30 minute behind the Landsat 7 system. Terra also carries four other sensors including the Moderate-resolution Imaging Spectro-radiometer (MODIS)

The ASTER instrument is provided by the Japanese government under the ministry of International Trade and Industry (MITI). Implementation is through non-profit organizations; the Earth Remote Sensing Data Analysis Center (ERSDAC) in Tokyo and the Japan Resources Observation System Organization (JAROS).

The ASTER sensor has three subsystems (see Table 1): the visible and near-infrared (VNIR) with 15 m resolution, short-wave infrared (SWIR with 30m resolution, and thermal infrared (TIR) with 90-m resolution (Thorne et al, 1998). The band 3N refers to the nadir-looking band and the identical band, 3B, views with a separate telescope in the backward direction for the purpose of stereo imaging and DEM generation. The swath width is 60 km.

Aster operates in two distinct spectral regions: the solar reflective (VNIR and SWIR bands), where the measured radiance is reflected solar radiation, and the TIR, where radiance is due to thermal emission.

TABLE I
ASTER BANDS AND RADIOMETRIC SPECIFICATIONS

Subsystem (& detector type)	Band #	FWHM bandpasses	Radiometric resolution	Quanti-zation	1-σ calibration uncertainty
VNIR (Si-CCD 5000 × 4)	1	0.52-0.60	0.5%	8 bit	±4%
	2	0.62-0.69			
	3N, 3B	0.76-0.86			
SWIR (Cooled PtSi 2048 × 6)	4	1.60-1.70	0.5%	8 bit	±4%
	5	2.145-2.185	1.3%		
	6	2.185-2.225	1.3%		
	7	2.235-2.285	1.3%		
	8	2.295-2.365	1.0%		
	9	2.360-2.430	1.3%		
TIR (Cooled HgCdTe PC 10×5)	10	8.125-8.475	0.3 K	12 bit	3 K (200-024 K) 2 K (240-270 K) 1 K (270-340 K) 2 K (340-370 K)
	11	8.475-8.825			
	12	8.925-9.275			
	13	10.25-10.95			
	14	10.95-11.65			

1.2 Getting data and information from the internet:

Technical Information on ASTER pre-processing can be found at:
http://eospso.gsfc.nasa.gov/atbd/astertables.html
Level 1b ASTER data can be ordered from EOS data gateway:
http://edcimswww.cr.usgs.gov/pub/imswelcome/
On demand products can be ordered from:
http://edcdaac.usgs.gov/asterondemand/

1.3 Previous examples of ASTER analysis

As the system is relatively new, there are relatively few case studies as yet to report on. This will certainly change in the near future. Hewson et al (2001) used simulated ASTER data (from HYMAP Mk1 and TIMS) to study the Mt Fitton area to map carbonates, chlorite, white mica and talc. The 6 SWIR bands (4-9) and the thermal IR data (bands 10-14) were processed separately. The SWIR data was processed with log residuals (to compensate for atmospheric effects) and then analyzed with MTMF. The end-members were apparently derived using automatic MNF processing although this is unclear. Certainly previous knowledge of the area mineralogy was useful in interpretation and analysis. The thermal data was presented as colour composite images of decorrelation stretch processing of raw bands 13, 12 and 10 in RGB. This delineated quartz, clay and talc rich areas.

1.4 Aim of this work

It is clear that there is a need for demonstrated examples of ASTER analysis. Currently the user is confronted, not only with unfamiliar data, but also with a confusing array of potential methodologies and software, many of them involving an expert knowledge in remote sensing. One shortcoming in the many courses and manuals on image spectral data processing is the lack of ground truth information. One aim of this project was to investigate the available methods of ASTER analysis for areas that have known mineral distributions. The first area investigated in this study (Indee, Pilbara, Western Australia) has been analyzed with airborne hyperspectral data, ground spectral work and XRD studies (Bierwirth et al, 2002).The second area, Laverton, W.A., is the subject of a recent map release (Stewart, 2001). It was thought that these two areas should provide important information about the capability of ASTER to map minerals and geological features.

2.0 Radiometric data correction of ASTER data.

Radiometric correction of radiance data is necessary to make comparisons with spectral properties of materials and to correct for often unwanted component in the data such as atmospheric components and temperature in thermal infrared (TIR) data. For the reflected solar-radiation bands in the VNIR–SWIR (bands 1-9), the ideal product is surface reflectance. For the TIR, it is desirable to have spectral emissivity data to analyze.

2.1 VNIR – SWIR apparent reflectance

2.1.1 ASTER level 2 on-demand reflectance data

Atmospheric correction of VNIR – SWIR data is available via on-demand (AST_07) processing of level 1B ASTER data (Thorne et al, 1998). The correction relies on inputs from other satellite sensors to determine the atmospheric characteristics of the scene to be corrected. These other sensors include the Multiangle Imaging SpectroRadiometer (MISR) and the Moderate Resolution Imaging Spectroradiometer (MODIS). The method is based on a lookup table (LUT) approach. Using the atmospheric inputs from other sources, a set of piecewise linear fits are determined from the LUT that relate the radiance at the sensor to surface radiance and reflectance. Atmospheric transmittance is estimated using the MODTRAN program and the satellite radiances are divide by these values. The scattering optical depths and aerosol types are obtained from climatology, MISR or MODIS and input to the LUT. For a typical 60 x 60 km ASTER scene, atmospheric composition is assumed constant for 5 x 5 km areas. A digital elevation model (DEM) is used in the calculation of scattering optical depth and the spatial resolution can be a limitation for accuracy of the correction. The product release-notes state that it is expected that DEMs with spatial resolution better than 100 m will be available but this is unlikely at present for many areas in Australia. There is no indication of what DEM is used for various areas. The lowest resolution will be a 1 km DEM which will create a noticeable artifact in the corrected data and this problem will be more visible in areas of strong relief.

The following statements are taken from the release notes at
http://asterweb.jpl.nasa.gov/products/Ast07_v2.3.pdf

Bands that are more affected by atmospheric absorption will have poorer accuracies due to uncertainties in the correction for these effects as well as uncertainties in the input parameters needed to correct for these effects. Bands where these effects are most important are Bands 6-9. All bands except band 1 have significant absorption effects, but these effects in bands 2-5 are either readily characterized or small enough that uncertainties in both inputs and treatment of the absorption will be minimal. For regions of high humidity, the uncertainties in this band can be more than 20% over bright surfaces. The effect is small over dark objects. The primary limitation to this product is the lack of aerosol correction. This has been done so as to create a product corrected for solar zenith angle changes and gaseous absorption, but not to overcorrect for the unknown aerosol inputs. Thus, the current data product will always overestimate the surface reflectance and surface radiance.

2.2 Thermal Infrared

2.2.1 Principles

Any object having a temperature greater that absolute zero (0 K or –273 degrees C) emits radiation. For a perfect blackbody, the amount of emitted radiation at a given wavelength interval is exponentially proportional to temperature given by Planck's Law:

$$L_{bb} = C_1 / \lambda^5 \pi (e^{c2/\lambda T} - 1) \qquad (1)$$

Where:

L_{bb} = blackbody radiance
L = wavelength,
T = temperature of the surface
C_1 = first radiation constant
C_2 = second radiation constant

In reality materials are not perfect blackbodies and the radiance is modified by the emissivity of materials ε which may vary depending on wavelength. The radiance emitted from the surface is:

$$L = \varepsilon L_{bb} \quad (2)$$

Atmospheric components also effect the radiance received at the sensor and the effect of these can be seen in the following equation:

$$L_s = [\varepsilon L_{bb} + (1-\varepsilon)L_d]\tau + L_u \quad (3)$$

Where:
L_s = the radiance measured at the sensor,
L_d = the downward radiance reflected from the surface toward the sensor
L_u = the upward radiance from the atmosphere

All of these parameters may vary according to wavelength. Incident radiance emitted from adjacent scene elements can also be important (Gillespie et al 1998). The emissivity of the surface is the parameter that is of interest for geological mapping because this property is characteristic and invariant for the various minerals and rock-types. In general mineral emissivities are in the range 0.8 – 1.0 (Lillesand and Kiefer, 1999) and consequently temperature tends to dominate radiance data in TIR bands. In order to directly compare remotely sensed TIR data to laboratory derived mineral emissivities, techniques must be employed to separate temperature and emissivity effects in image data. Assuming that the atmospheric components can be removed, the relationship described represents an under-determined situation, i.e. N bands for solving N + 1 unknowns (N emissivities + temperature).

2.2.2 Techniques for deriving emissivity

Early methods involved assuming a constant emissivity for one band, calculating the temperature from equation 1 and then solve emissivity in all the other bands (Kahle and Alley, 1992). This is known as the "reference channel method". The wavelength commonly used is 11.75 μm where emissivities are near 0.95 for silicate rocks. Carbonate emissivities are much lower and then the assumption is no longer valid although the technique preserves spectral shape rather than amplitude. Another method involves fitting the Planck blackbody curve to radiance values so that is curve fits above the data values. The temperature is determined from this curve and then emissivities calculated from equations 1 and 2. This is the "blackbody fit" method (Kahle and Alley, 1992). The normalized emissivity method (NEM) calculates temperatures using a constant emissivity value (e.g. 0.96) for each channel. The highest of these are then used to calculate emissivities.

Log Residuals (Hook et al, 1992) and Alpha Residuals (Kealy and Hook, 1993) both isolate emissivity information but not temperature data using logarithms and Wien's approximation (neglecting the –1 term in equation 1). Log Residuals use band means (over all pixels for a single band) and pixel means (over all bands for a single pixel) while Alpha Residuals use pixel means. Watson (1992) uses spectral ratios to overcome the problem of temperature dominance in thermal images. The problem with Log Residuals, Alpha Residuals and ratios is that they cannot be directly compared with laboratory measured emissivities of materials although these can often be converted. Kealy and Hook (1993) suggest that emissivity can be reasonably approximated from alpha residuals by using a mean emissivity (between bands) estimated from a standard relationship between this mean and the variance of the alpha residuals

All of these techniques described require data corrected to radiance leaving the surface (i.e. atmospherically corrected). Log Residuals is a method that could be used without atmospheric correction although for thermal data, although the upward atmospheric radiance component in equation 3 can be quite large (Hook et al, 1992) and may cause errors such as a change in spectral shape for materials with similar emissivity properties but different temperatures. Kay et al (2001) describe a technique which derives relative atmospheric gains and offsets by regression of image data for a material with known emissivity, e.g vegetation.

More simple techniques can be used for image enhancement without the need for complex processing or atmospheric correction. Colour ratio compositing can allow the information from six bands to be displayed in a single colour image and this suppresses the correlated temperature component. Another commonly used technique is decorrelation stretching (Gillespie, 1992). In this method, image data is transformed to Principal Component (PC) space, each band is separately contrast stretched and then transformed back to the original space. This has the effect of enhancing emissivity information as highly saturated hues. Temperature information is still preserved, however, as intensity information (Kahle and Alley, 1992) and Gillespie (1992) argues that temperature data often contains useful terrain information.

Other simple techniques using the ASTER TIR bands are proposed by Ninomiya and Fu (2001). Ratios for silica (b11*b11/b10/b12), carbonate (13/14), basic degree index (12/13) were deemed successful. In this study, the standard decorrelation stretch 13, 12, 10 (as RGB) also appeared to perform nearly as well.

In general there is a lack of studies that compare the general success of these strategies for processing TIR data.

2.2.3 ASTER Level 2 - The TES algorithm

The Temperature Emissivity Separation (TES) algorithm is the method selected by the ASTER science team to extract the temperature and 5 emissivities from the 5 TIR channels of ASTER (Gillespie et al, 1998). Currently it is possible to order (and receive quickly via ftp) the TES products via the Internet by specifying any existing level 1B ASTER granule number. Release notes for the on-demand product are found at: http://asterweb.jpl.nasa.gov/products/release_surface_emissivity_product.htm
The method involved a number of steps and processes:

1) Initially the L1B data is converted to radiance (still haven't found any documented conversion factors) and then corrected for atmospheric transmission and path radiance (τ and L_u respectively in equation 3 above). These atmospheric parameters are derived from the MODIS instrument collected from the EOS-AM1 platform at around the same time of ASTER acquisition (Palluconi et al, 1996). There may be complex patterns of inaccuracies due to the relative coarseness of the MODIS spatial resolution (Gillespie, 1998).

2. The TES algorithm uses the normalized emissivity method (NEM) described above to initially estimate temperature for each band using equations 1 and 2 above. A ε_{max} of 0.99 is used and emissivities are calculated for each band. If the variance in emissivity is low then the surface is likely to be nearly a blackbody (e.g. vegetation). If the variance in ε values is high then the pixel is probably a rock or soil and the ε_{max} value is assumed to be 0.96 and the process is restarted. The process is used iteratively to recalculate ground emitted radiance (L), temperature (T) and ε until the changes in L becomes small. This has the effect of correcting for the effects of downwelling atmospheric radiance (L_d) on pixel radiance.

3. The next step is the ratio module (Gillespie et al, 1998) which is effectively the alpha residuals technique described above (Kealy and Hook, 1993). The relative emissivities are ratioed to their average across all bands. The reason for this step is not well explained by Gillespie et al (1998) particularly since it removes the amplitude of emissivity spectra. The next step restores emissivities by introducing a constraint so that the authors clearly believe that the emissivities and temperatures derived by NEM and step 2 above are inadequate.

4. The alpha residuals are converted back to emissivity by the use of an empirical relationship between (1) the difference between minimum and maximum alpha residuals and (2) the minimum emissivity if natural materials. This relationship has been established from laboratory reflectance spectra of a range of materials. This is effectively the constraint that allows the solution of an underdetermined set of equations. The scatter in this relationship is potentially a source of error in the solutions but Gillespie et al (1998) believe that the constraint is better than the assumptions used in other algorithms.

5. The TES ε values are then used to make a single correction to L, followed by step 3 and 4 to produce final ε and T values.

3.0 Evaluation of ASTER data: application to case study areas.

3.1. Study site 1: Indee, Pilbara, W.A.

3.1.1 Introduction

The aim for this site was to assess the ASTER data for an area that already has been surveyed by high-resolution airborne hyperspectral data together with extensive fieldwork including (1) geological mapping and spectral characterization. Spectral

work included analysis of field samples using the Portable Infrared Mineral Analyser (PIMA) and the FieldSpec Analytical Spectral Devices (ASD). The PIMA measures reflectance from 1.3 to 2.5 μm while the FieldSpec ASD® measures the same from 0.35 to 2.5 μm.

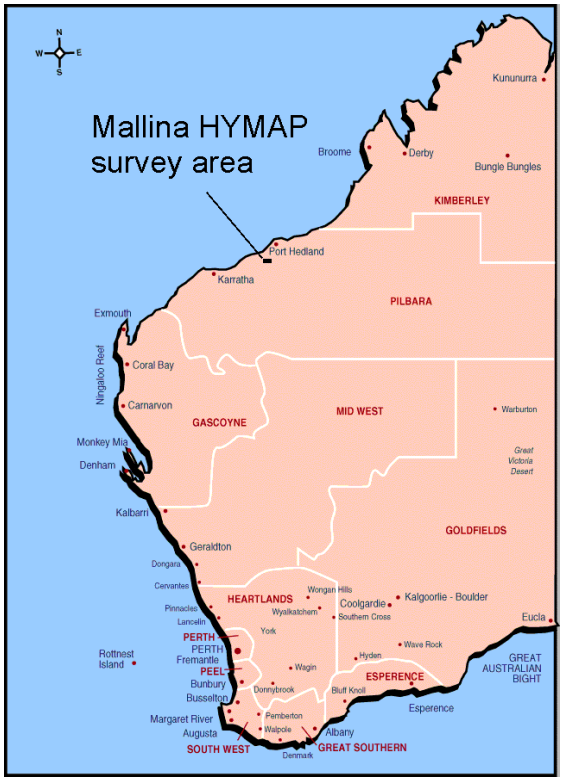

Figure 1. Location of the Indee (Mallina) Pilbara site.

The Indee district, located in the Central Pilbara Tectonic Zone of the North Pilbara Terrane in Western Australia (Figure 1) contains Archean lode gold deposits and epithermal gold systems. Host rocks are metasediments and basic igneous rocks. Hydrothermal alteration assemblages associated with these deposits contain the minerals pyrophyllite, white mica, chlorite and tourmaline. Known prospects are surrounded by flat areas of poorly exposed, calcretized bedrock, calcretes, rock float and sandy soils. Two adjacent lines of airborne hyperspectral data (HyMap®) were acquired. Analysis of these data are described in Bierwirth (2000) and Bierwirth et al (2002).

Level 1B ASTER data was ordered via the EOS data gateway (see section 1.2) Reflectance and emissivity data were ordered from the USGS web site after specifying the ASTER scene granule number. Once notified by email, all data were downloaded by ftp. The resulting HDF files can be read by both ERMapper and ENVI software packages although ERMapper 6.1 failed to read HDF files generated for the on-demand products, i.e. reflectance and emissivity. In the latter case, the data were read into ENVI before converting to ERMapper files prior to registration.

3.1.2 Geometric correction

In order to directly compare the ASTER to the HYMAP results, it was necessary to perform an image to image registration. This will be more accurate, for a direct comparison, than map registration for both data sets. 60 control points were collected from the ASTER VNIR data (15 m pixels) and similar bands from the airborne HYMAP (10m pixels) and triangulation was used as the rectification method. This was all performed in ERMapper. Generally errors were within two pixels and results were much better than linear and quadratic polynomial warps.

In many cases, it may not be necessary to collect control points to register ASTER data. Some workers have found that the ASTER data has relatively good spatial accuracy when imported into ENVI and system parameters are entered (R. Hewson, K. Pfitzner, pers. comm.). This needs to be properly investigated.

3.1.2 Cloud Masking

Cloud areas were visually identified in VNIR data (i.e. an RGB composite of bands 3,2 and 1 respectively) and regions of interest (ROI's) were drawn to characterize both cloud tops and cloud shadows. Signatures from reflective bands (1-9) were collected from these ROI's and matched filtering (the method is discussed later) was used to attempt to identify cloud affected areas. Cloud shadows were best identified with all 9 bands whereas the cloud-tops were indistinguishable from many bright surfaces. This is characteristic of this particular area where calcretes form particularly bright spectra. For this data and because it was a small scene, it was possible to hand-draw ROI's for the cloud-tops. This is contrast to the Laverton study area (see section 3.2.2) where it was possible to derive an image generated cloud-top mask. The ROI's for both cloud-tops and cloud shadows were then used to create a cloud mask.

3.1.3 Comparisons with Landsat TM

Figure 2 shows a comparison of similar bands for Landsat TM and ASTER data sets for the Indee study area (the 16 km x 8 km overlap area between ASTER and HYMAP data). In this combination, clay tends to be red, green vegetation is green and Fe-oxide dominated areas are blue. The date of acquisition of the Landsat image is unknown but is from the AGSO collection and used for the Pilbara project and would be many years old. The ASTER scene was acquired on 20 December, 2000. The difference between the scenes is significant and they both show extensive fire-burn histories. The TM scene shows larger areas of dark woody vegetation and perhaps burnt since there is only a very low NIR reflectance. The strong presence of Fe-oxides (blue colours) in the sandy areas suggests a lack of vegetation and general dry conditions. In contrast, the ASTER has less dark vegetation but has a green tinge across the scene, suggesting fairly recent rains, but cut across by recent bush-fires exposing Fe-oxides (blue areas). The ASTER data is consistent with TM data when viewed at similar spectral and spatial resolution.

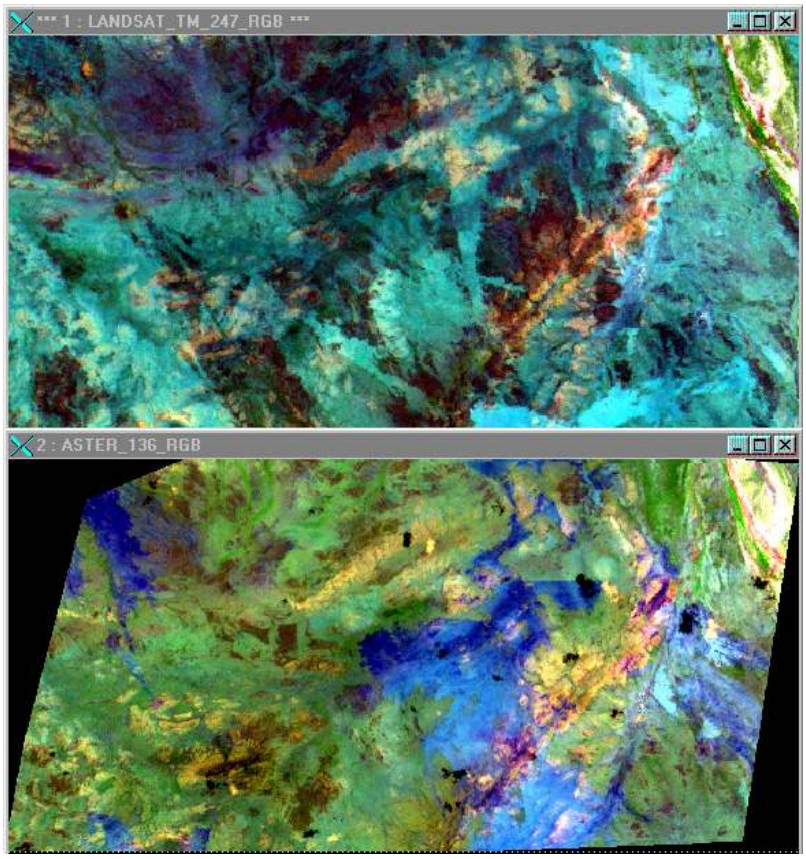

Figure 2. Comparison between (top) Landsat TM bands 2,4 and 7 as RGB respectively and (bottom) comparable ASTER level 1B bands 1, 3 and 6 as RGB. (16 x 8 km area).

Figure 3 is a zoomed in 1.5 x 2 km sub-area of Figure 2 showing the improved spatial detail in ASTER visible and near-infrared (VNIR) bands 1 and 3 (the red and green components of the image on the right).

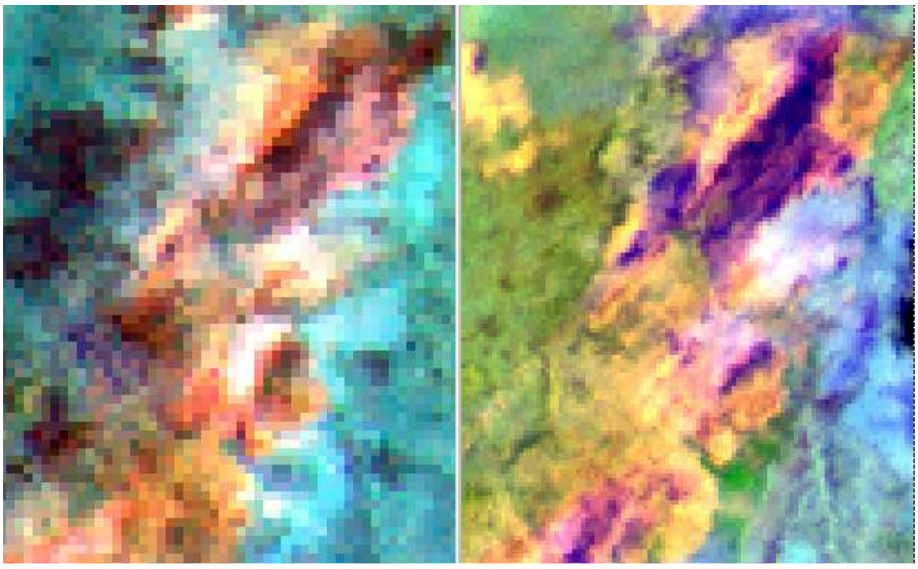
Figure 3. Comparison of the same data in Figure 2 for a 1.5 x 2 km sub-area.

The main improvement of ASTER over Landsat TM is the increased spatial resolution in the short wave infrared (SWIR). Landsat TM has only band 7 in this spectral region

(2.08 – 2.32 μm) and ASTER has 5 bands in the range 2.145 – 2.430 μm. Figure 4 shows a comparison between a single greyscale Landsat band 7 (bottom), simulated from ASTER bands 5-8, and a Principal Components image generated from 5 of the ASTER SWIR bands. Broadly, clay areas show as green and carbonates as magenta to blue. It is worth noting the large influence of vegetation in the spectral variability of the SWIR bands and the problems this poses for the spectral identification of minerals.

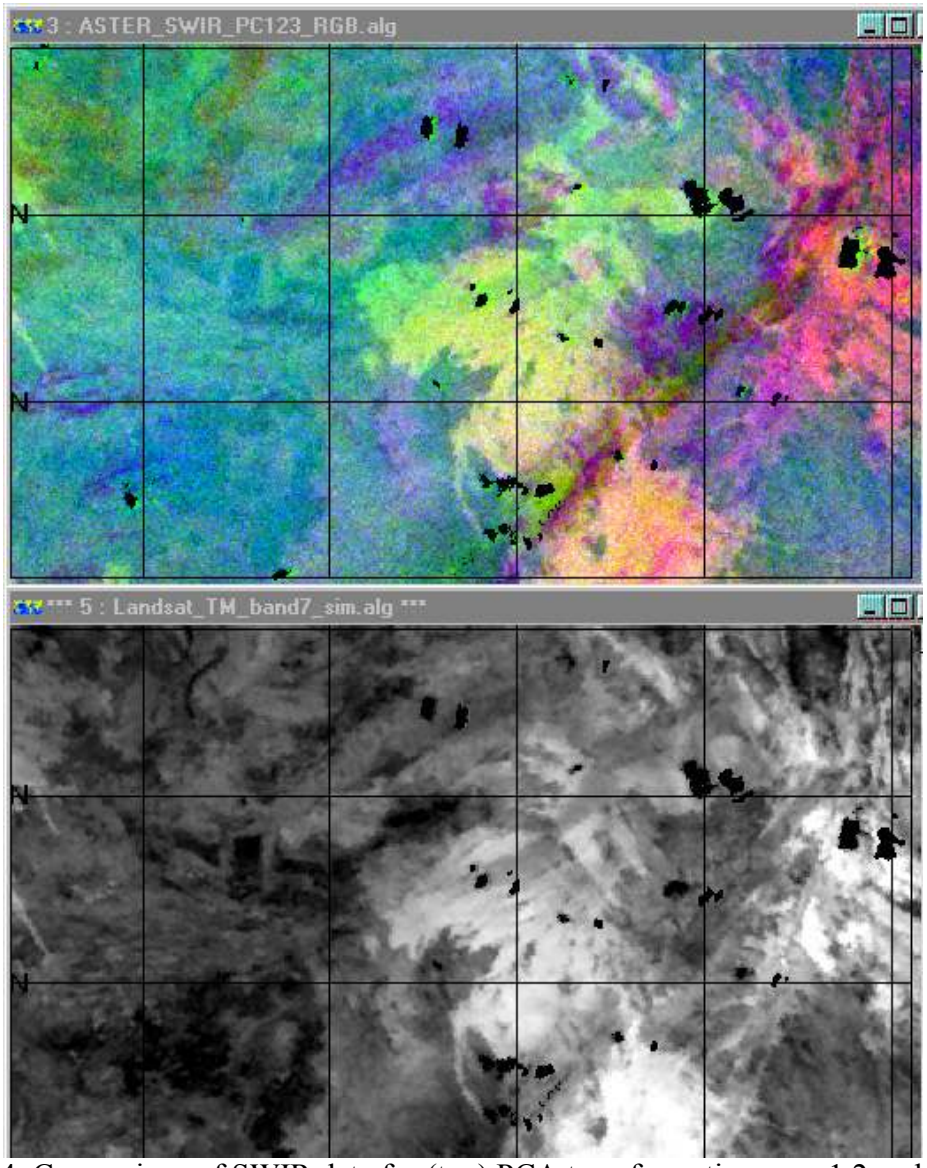

Figure 4. Comparison of SWIR data for (top) PCA transformation axes 1,2 and 3 as RGB (generated from ASTER bands 5-9) and (bottom) Landsat TM band 7 (grid cells are 2.5km).

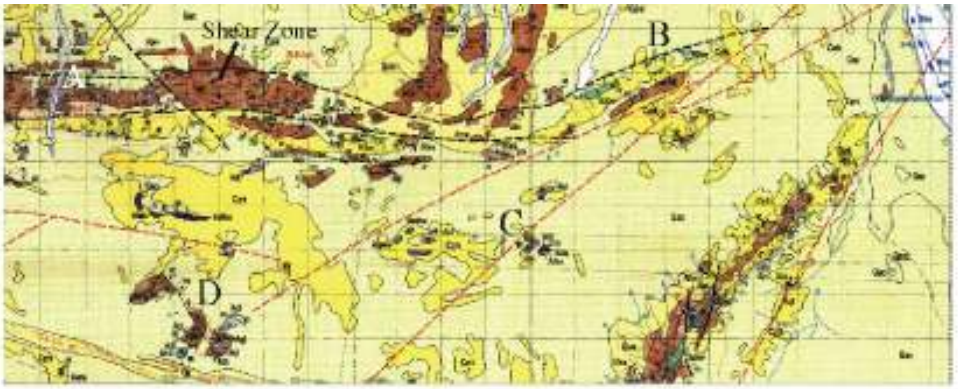

Geology of the Mallina HYMAP survey area. Brown areas are metasediments of the Archaean Mallina Formation. Green and purple units are mafic to ultramafic igneous rocks. Bright yellow areas are calcrete, paler yellow areas are sandy soil. (From Smithies, 1999) Grid lines are at 1 km.

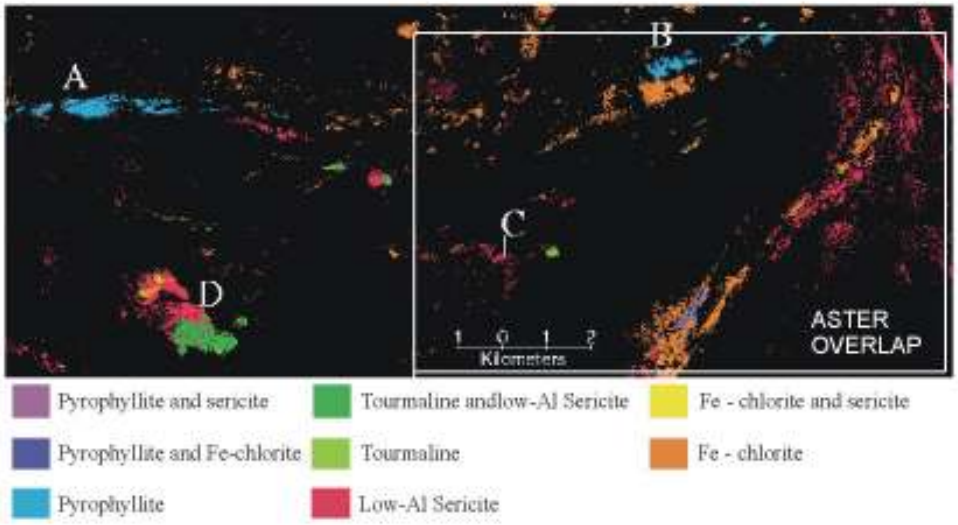

Airborne hyperspectral mapping of minerals associated with gold and hydrothermal alteration

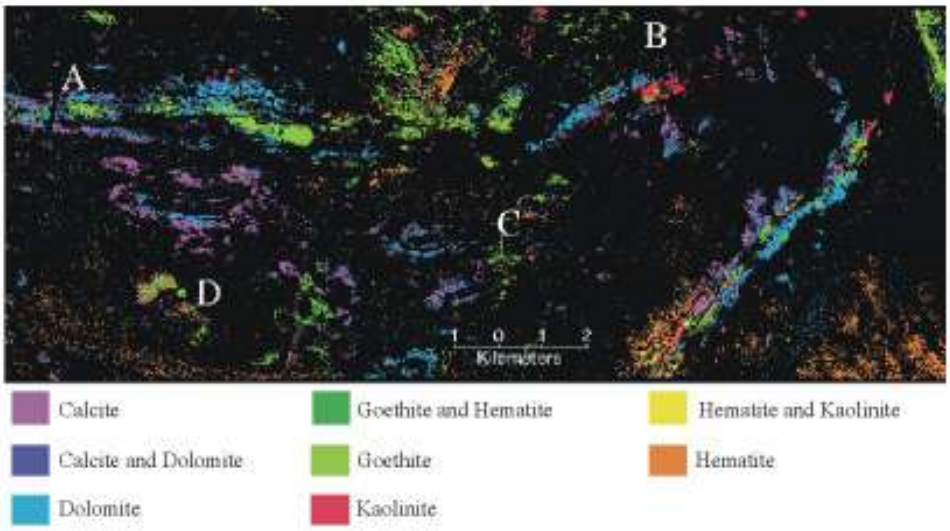

Airborne hyperspectral (HYMAP) mapping of regolith and weathering minerals

Figure 5. The Indee area (top) geology, (middle) hydrothermal minerals, and (bottom) regolith minerals as measured by analysis of airborne hyperspectral HYMAP data.

3.1.4 Airborne hyperspectral HYMAP data – target minerals

The airborne HYMAP data has been processed to correct for atmospheric and illumination conditions and then calibrated to reflectance data using field spectra (Bierwirth, 2000; Bierwirth et al 2002). The data were then processed to produce mineral abundance images. This analysis successfully mapped the distribution of pyrophyllite, two types of white mica, Mg-chlorite, Fe-chlorite, calcite, dolomite, kaolinite, tourmaline, hematite and goethite. These were a combination of hydrothermal, metamorphic and in-regolith minerals.

Only the eastern half of the HYMAP acquisition area was covered by existing ASTER data. Figure 5 shows results of the HYMAP analysis with the boxed area in the middle image showing the extent of ASTER data overlap. Mineral assemblage and mineral maps created from the HYMAP data were produced from unmixed mineral-abundance images with thresholds applied (Bierwirth et al, 2002).
The spectra in Figure 6 are all measured with the PIMA from samples within the high abundance areas (with the exception of the kaolinite spectrum which is from the USGS spectral library). They represent nearly pure materials in the Indee area, These materials have been quantified across the area using airborne hyperspectral data and it is possible to investigate whether ASTER is capable of the same. The right hand of Figure 6 shows the PIMA spectra resampled to ASTER wavelengths. While there are clear differences, it is unclear whether it is possible to resolve these minerals at ASTER resolution.

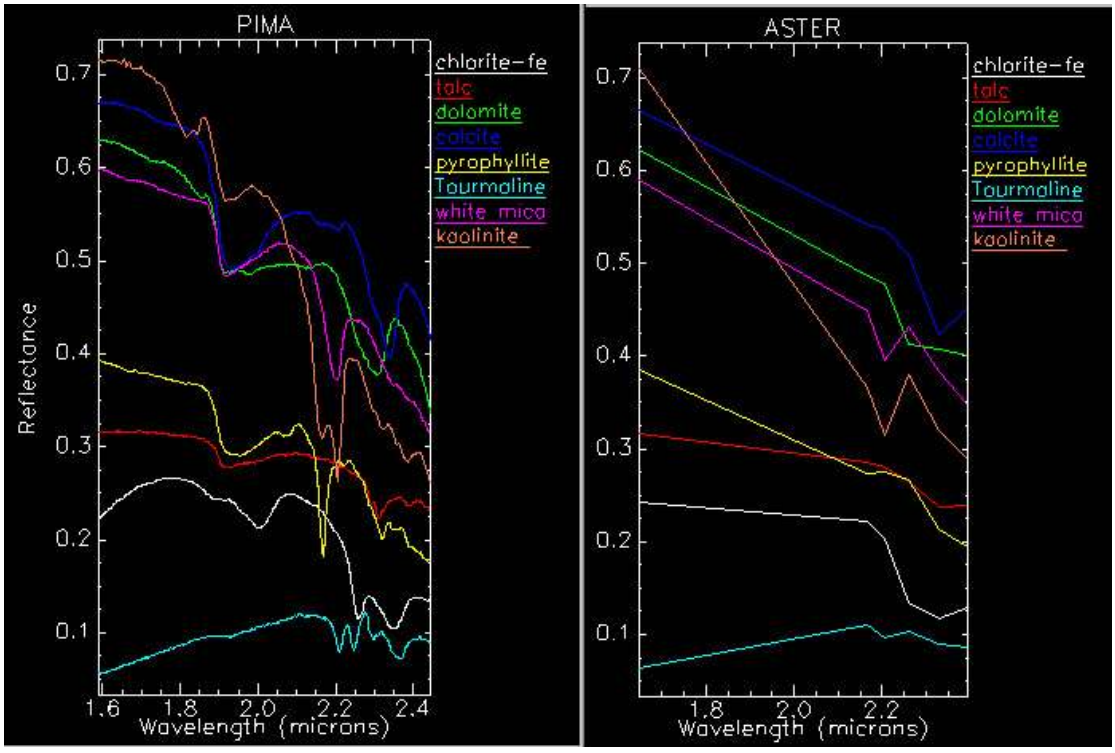

Figure 6. Minerals of the Indee, Pilbara area: (a) PIMA spectra (b) convolved to ASTER wavelengths

3.1.5 Conversion of ASTER data to relative reflectance

The HYMAP data were corrected to reflectance using the ATREM and EFFORT procedures as contained in the HYCORR program (Bierwirth, 2000). Another method was also employed to correct spectral shape by using ground spectra. This method, called reflectance-mean normalisation (RMN), involves modifying band gains by using a scene reflectance-mean. This mean is estimated from ground spectra from across the scene. ATREM employs the use of narrow water absorption bands at 0.940 and 1.140 μm to correct for water vapour and this is not feasible with the spectral resolution of ASTER. Three techniques were investigated for ASTER:

1) ASTER Reflectance product (AST_07) (Thorne et al, 1998) – see description above in Section 2.1.1.
2) A flat field correction which assumes a flat spectrum in the SWIR for a calibration target (in this case cloud)
3) RMN conversion based on calibration the data to field spectra.

The last two methods both involved subtracting a dark pixel value in the VNIR bands to remove the path radiance (atmospheric backscatter) component of the data.

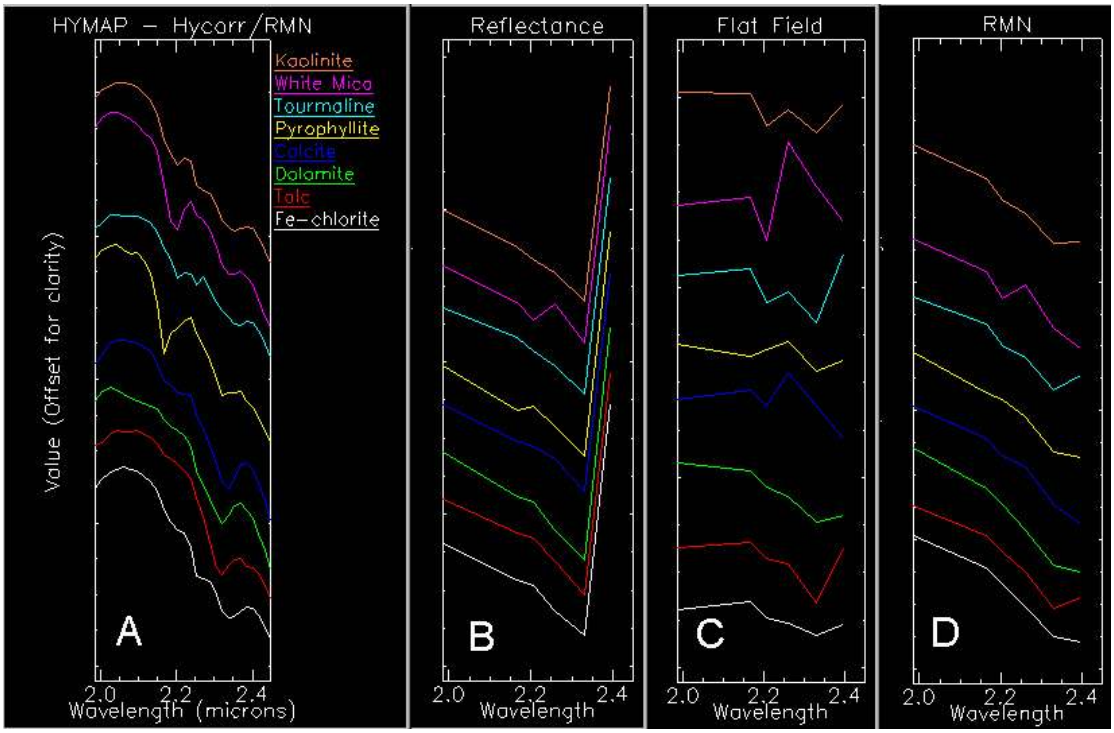

Figure 7. Average spectra for areas of high mineral concentrations as identified by (A) HYMAP calibrated to reflectance and 3 different ASTER calibrations (B) Level 2 reflectance (C) Based on Flat Field reflectance of clouds and (D) RMN reflectance.

3.1.6 Comparison of HYMAP and ASTER mineral signatures

Since the images are registered it is possible to make a comparison of HYMAP and ASTER spectral data. To do this, both data sets need to be converted to reflectance - this will be discussed further below. Regions of interest were drawn for HYMAP mineral abundances (an average of the highest 50 pixels) in homogeneous areas but inside these by a distance of at least two pixels - as mentioned earlier there can be an error in registration of up to two pixels. Average ASTER spectra were collected for

the areas of high mineral abundances and these are shown in Figure 7 for the three methods of reflectance conversion. Figure 7(A) shows the HYMAP average spectra for the 100 highest pixel (10m resolution). The flat field data have greater contrast because the spectra are flatter probably since clouds will have gradually reduced reflectance with longer wavelength. The AST_07 product reflectance has a major problem in band 9 centred at 2.395 while the RMN method appears in this case to correlate well to the HYMAP and realistic surface reflectance.

Given that there were problems with the AST_07 reflectance product, the mean of band 9 was adjusted so that it's ratio to the other SWIR bands was the same as the RMN corrected data. The multiplying factor was 0.598 and this is potentially a factor that can be used for other scenes. Examples of the corrected data can be seen in Figure 8 where the reflectance accuracy does seem reasonable.

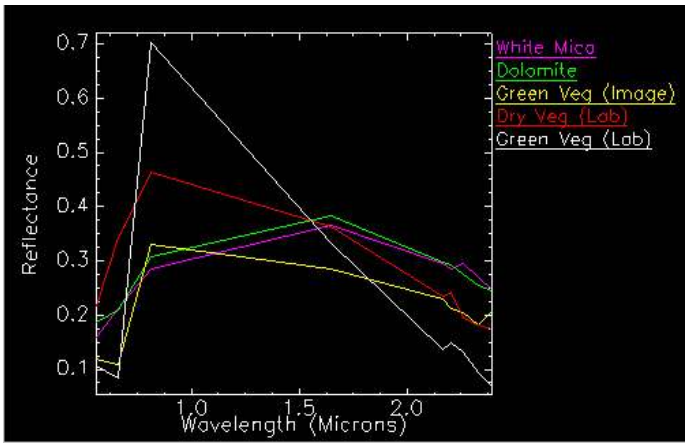

Figure 8. ASTER level 2 reflectance (product AST_07) with band 9 corrected – examples are average spectra from HYMAP high abundance zones of white mica, dolomite and green vegetation. These are compared with lab spectra for vegetation, both green and dry.

Later work on the Laverton area (see section 3.2.5) highlighted a problem with the level 2 reflectance data, particularly in bright areas where a strong 2.165 (band 5) absorption feature is present and completely unrealistic for the area. Figure 9 shows a comparison of ASTER reflectance spectra for the burnt area (blue area in Figure 2-bottom) and cloud-tops using the two calibration methods; ASTER Level 2 and RMN described above. The burnt area is known, from fieldwork, to be composed largely of sandy soils dominated by hematite, kaolinite and quartz. The RMN spectrum for these areas is realistic showing a 2.2 μm feature and high reflectance in the SWIR. Similarly, the cloud-top RMN spectrum is also realistic with no features in the SWIR. The Level 2 data shows a 2.165 feature for both and this is an artifact of the processing. This is similar to the problem discovered in the Laverton data although apparently not as severe. In the following spectral processing step, the level 2 reflectance product was used, largely because this problem was not really identified until after the Indee work was done. Subsequent tests revealed that the RMN data produced only slightly better results. This is in contrast to the Laverton area where the RMN reflectance conversion clearly produced better results.

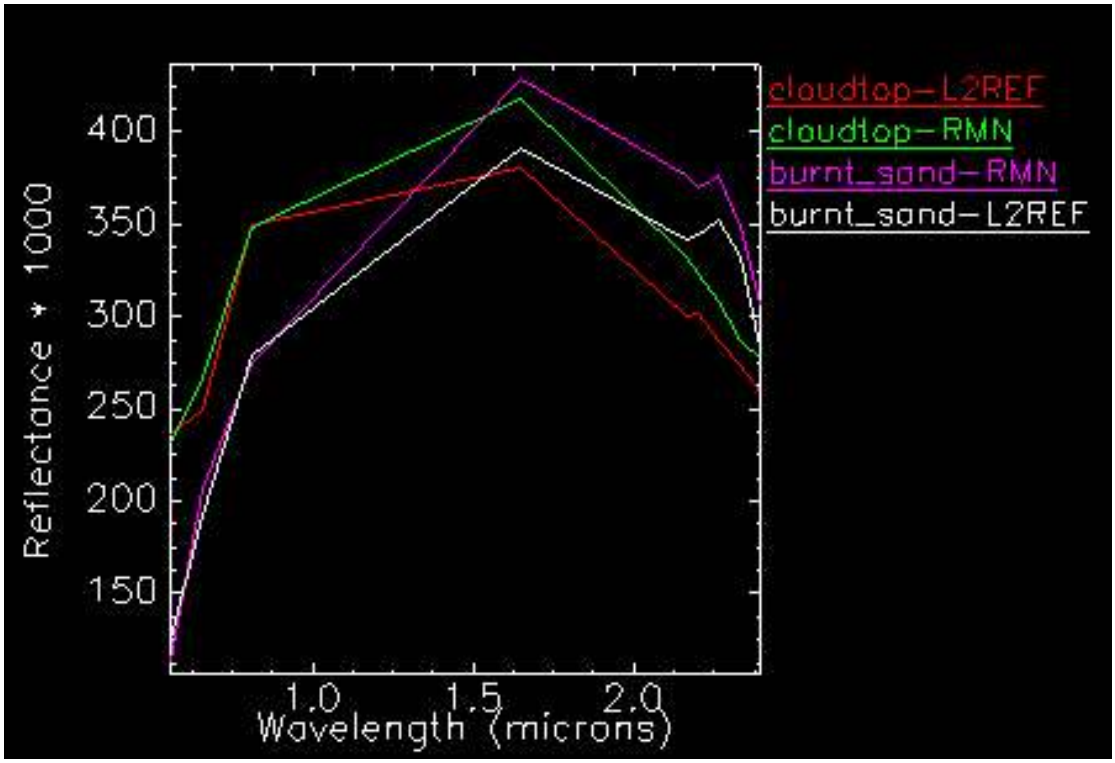

Figure 9. Comparison of reflectance spectra for the ASTER level 2 and Reflectance Mean Normalization (RMN) for cloud-tops and a high reflectance burnt area.

3.1.7 Mineral mapping using ASTER

3.1.7.1 Mixture tuned Matched Filtering (MTMF)

The matched Filtering method in ENVI is based on the partial unmixing technique (Boardman et al, 1995; Harsanyi and Chang, 1994) where the abundance of a given spectral endmember is calculated without direct reference to any other scene endmembers. In this process, a mixing vector is defined from the selected endmember itself and a second point that found using the background shape of the data cloud.

One way of analysing partial unmixing results is to examine infeasibility scores (Boardman et al, 1995). The infeasibility score represents the perpendicular distance between the pixel vector and the end-member vector. A high infeasibility together with a high abundance can indicate false commission in the results. Figure 10 shows an MTMF analysis of tourmaline abundance in the ASTER scene for the Indee test area. Tourmaline is a particularly difficult mineral component to extract given ASTER wavelengths. The image at top-left is the Matched Filter (MF) scores for the tourmaline end-member (the signature used was averaged from high concentration areas identified by HYMAP) compared with the HYMAP tourmaline abundance (top-right). Areas of high MTMF infeasibility in the scattergram (bottom-left) of score versus infeasibility can be identified and masked or coloured in the MF score image. As shown, the larger area of tourmaline (white, top-left image) is identified by its high MF score and low infeasibility. Other smaller areas of tourmaline in the northeast of the image may be too small to be clearly identified by ASTER.

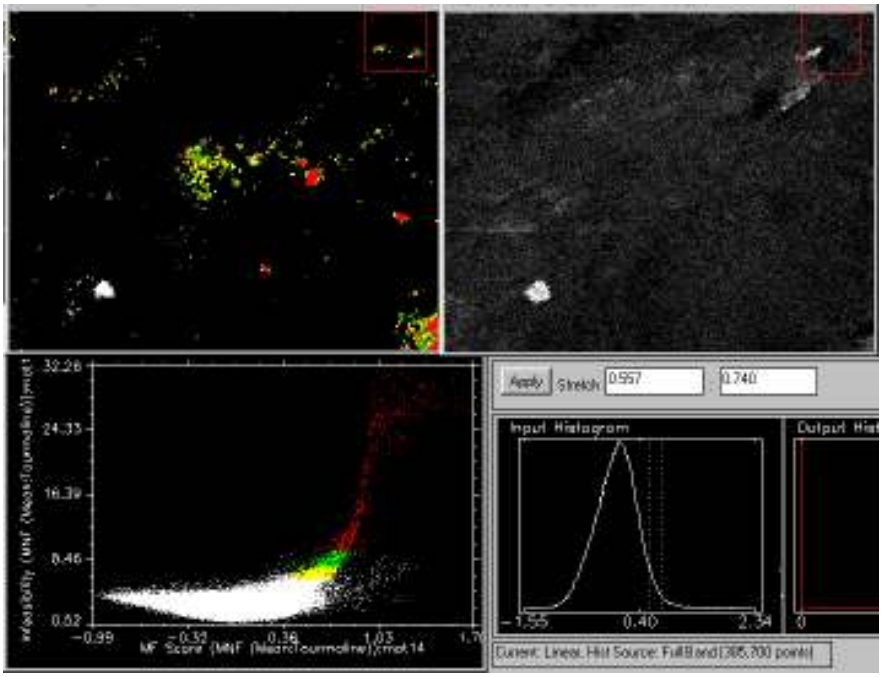

Figure 10. (Top-left) ASTER MTMF score for tourmaline coloured by MTMF infeasibility (top-right) HYMAP tourmaline abundance (bottom-left) scattergram of score versus infeasibility (bottom-right) histogram and stretch limits for the image at top-left.

The ASTER level 2 reflectance data was used as input to the MTMF process. Both the full VNIR-SWIR spectrum (bands 1-9) and just the SWIR (bands 4-9) were tested as input data. Spectral end-members were averaged from the ASTER data in the HYMAP defined regions for each target mineral (as described earlier). Some of these end-members worked better using the full 9 bands, others better with the SWIR and many were similar with both. This obviously depends on the spectral properties of materials and also the types of mixtures present. The level of accuracy of the processing was largely determined by the comparison with the HYMAP data.

Figure 11 shows MTMF results for pyrophyllite and tourmaline, both processed using bands 1-9 of the level 2 reflectance data. The ASTER pyrophyllite image is not working well although it appears that some pixels in the top-centre of the image are correctly identified. Probably the main reason for the inability of ASTER to detect pyrophyllite is that the 2.167 AlOH feature produces only a small feature in the broader band ASTER band 5 (2.145 – 2.185 μm). Signal to noise characteristics of the sensor may also be a factor. The tourmaline is also noisy but the large outcrop detected by HYMAP is also present in the ASTER data. As detailed above, the infeasibility score of the MTMF is crucial to being able to separate tourmaline areas

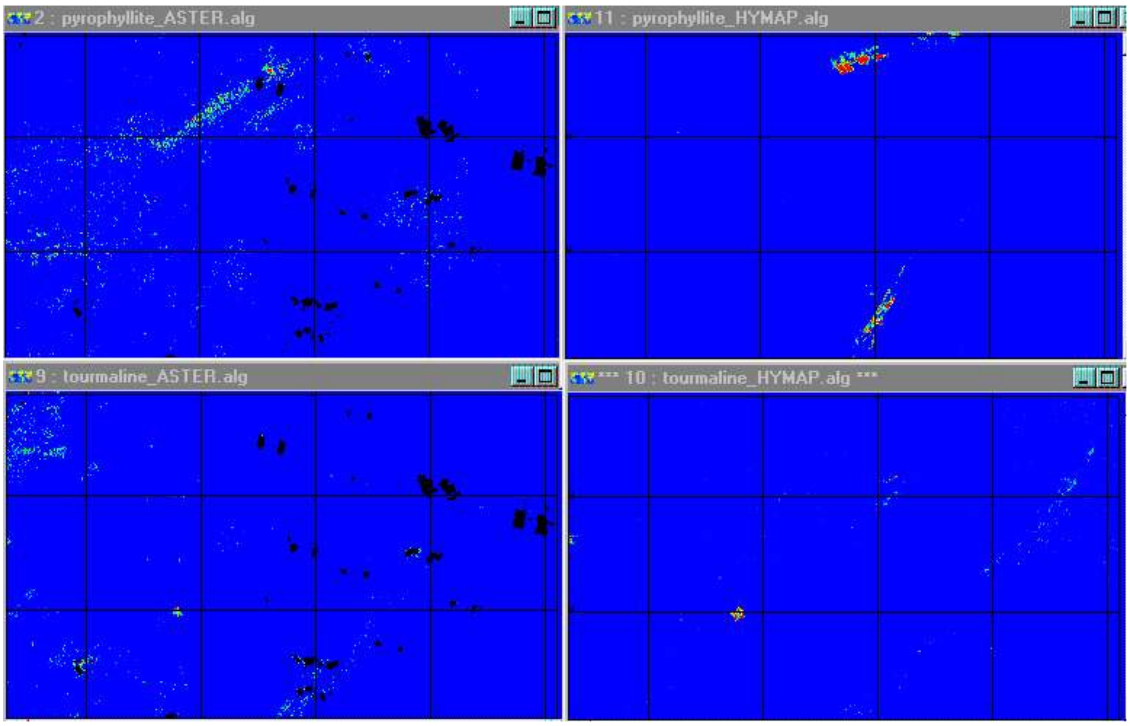

Figure 11. MTMF results for pyrophyllite and tourmaline comparing ASTER and HYMAP. Black areas are masked clouds. The area is 12 x 7 km. (grid cells are 2.5 km)

Calcite and dolomite images were generated using the VNIR and SWIR bands (Figure 12 – top and middle). In this case, there is a strong correlation between the ASTER calcite and dolomite images due to the lack of spectral separation of these minerals at ASTER wavelengths. In contrast, the HYMAP shows good separation of these minerals and this has been verified in the field (Bierwirth, 2000). The ASTER carbonate images show a larger area and this seems to be due to the over-zealous thresholding of the HYMAP data. There is a subtle difference in the ASTER data along the ridge in the southeast where dolomite is more abundant indicating that further processing might be possible to achieve calcite/dolomite separation. Along the same ridge, Fe-chlorite concentrations are observed in both the ASTER and HYMAP data (Figure 12-bottom). Other areas observed by HYMAP have been omitted in the analysis of the ASTER data and these areas correspond with areas of kaolinite weathering of chloritic bedrock in the lower landscape. It is believed that the resulting mixed spectra confuses the analysis of chlorite. Best results for chlorite were obtained using just the SWIR bands for this area.

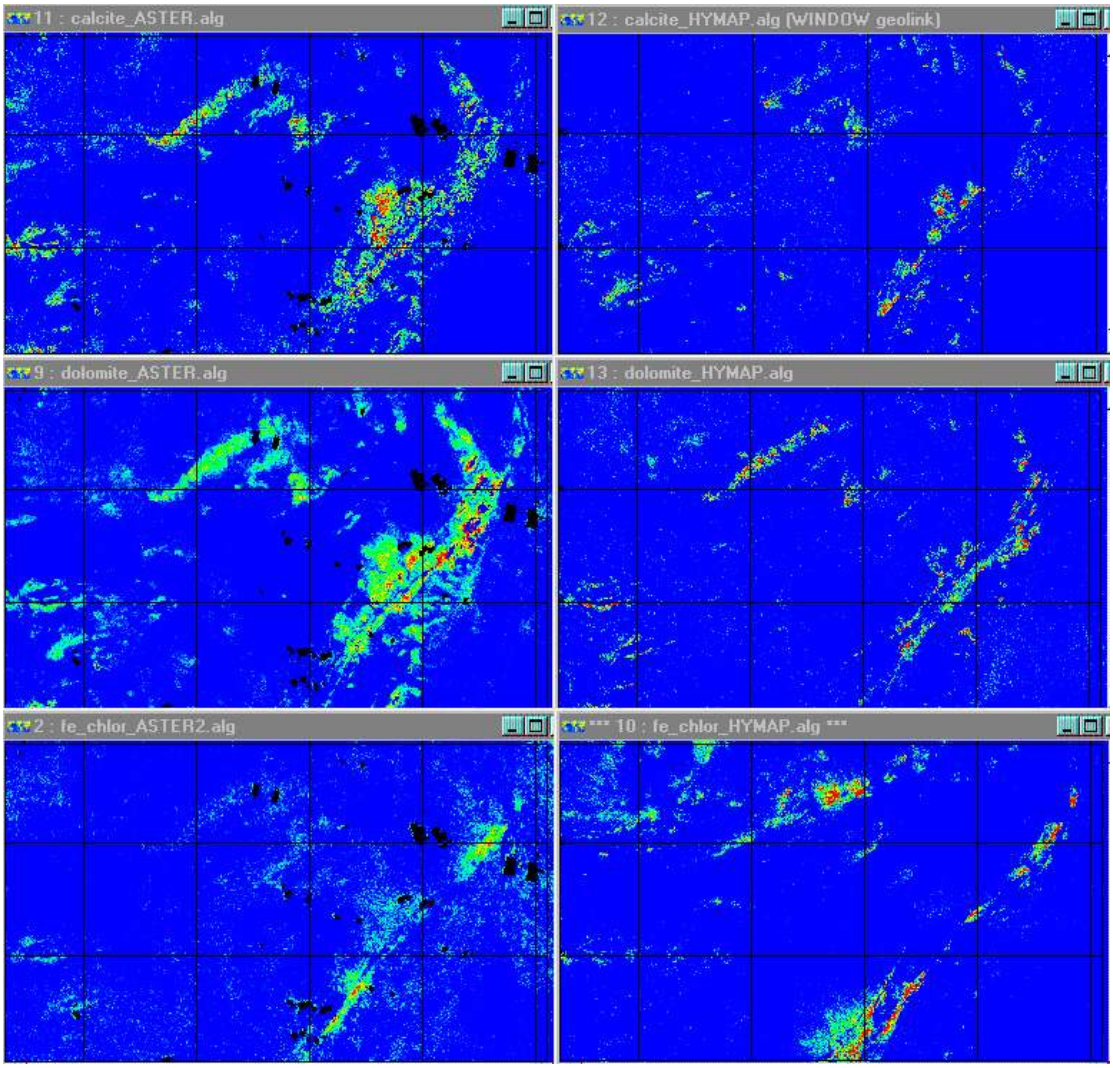

Figure 12. MTMF results for calcite, dolomite and Fe-chlorite: comparison of ASTER and HYMAP data.

White mica and kaolinite spectra are both dominated by the 2.2 μm feature (see Figure 13 – top and middle) and it was envisaged that separation of these minerals at ASTER wavelengths might be difficult. Figure 13 shows results from processing the combined VNIR and SWIR data, although similar results were obtained by using just the SWIR data. It appears that although considerable separation has been achieved, the white mica image shows high abundance kaolinite areas and vice-versa. Again further processing might be possible to improve this separation. The talc data (Figure 13 bottom) appears to indicate a good match between the ASTER and the HYMAP data, although there is still some noise.

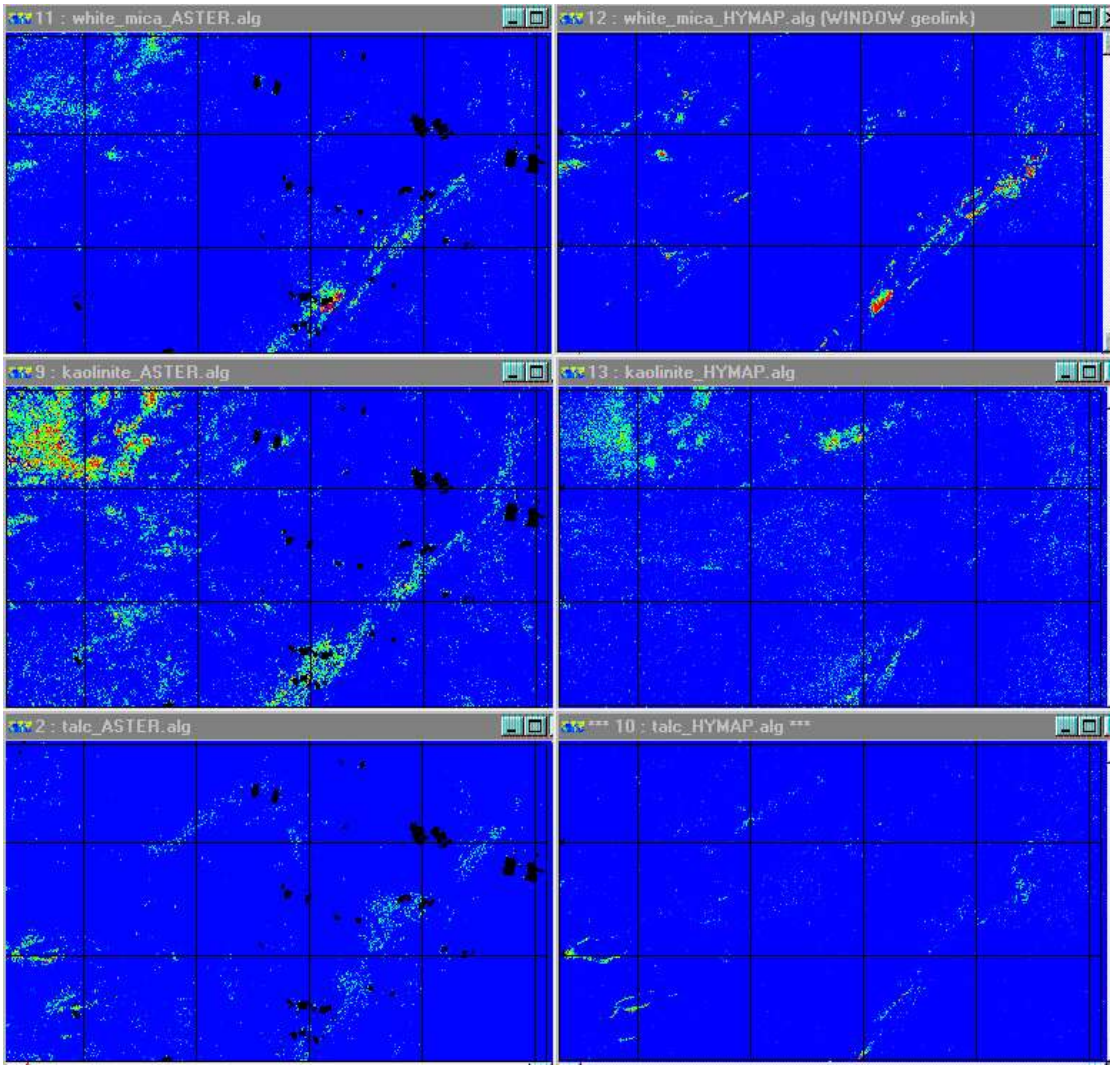

Figure 13. MTMF results for (top) white mica, (middle) kaolinite and (bottom) talc - comparison of ASTER and HYMAP data.

The ASTER hematite and goethite images (generated from the 9 VNIR-SWIR bands) (Figure 14) are almost identical and appear to be mapping mostly goethite as detected by the HYMAP data. The reason for the similar images is that the signatures derived from the ASTER data for goethite and hematite were very close, as would be expected at ASTER spectral resolution. But it is unclear as to why the Fe-oxide end-member has not mapped the hematitic areas identified by HYMAP which detects hematite by the discrimination of the 0.86 feature. In the study area, hematite is commonly mixed with kaolinite (although often below the threshold set for kaolinite in Figure 5 - bottom) in the weathered and leached sandy soils and it is possible that these mixed areas are preventing ASTER identification of hematite areas.

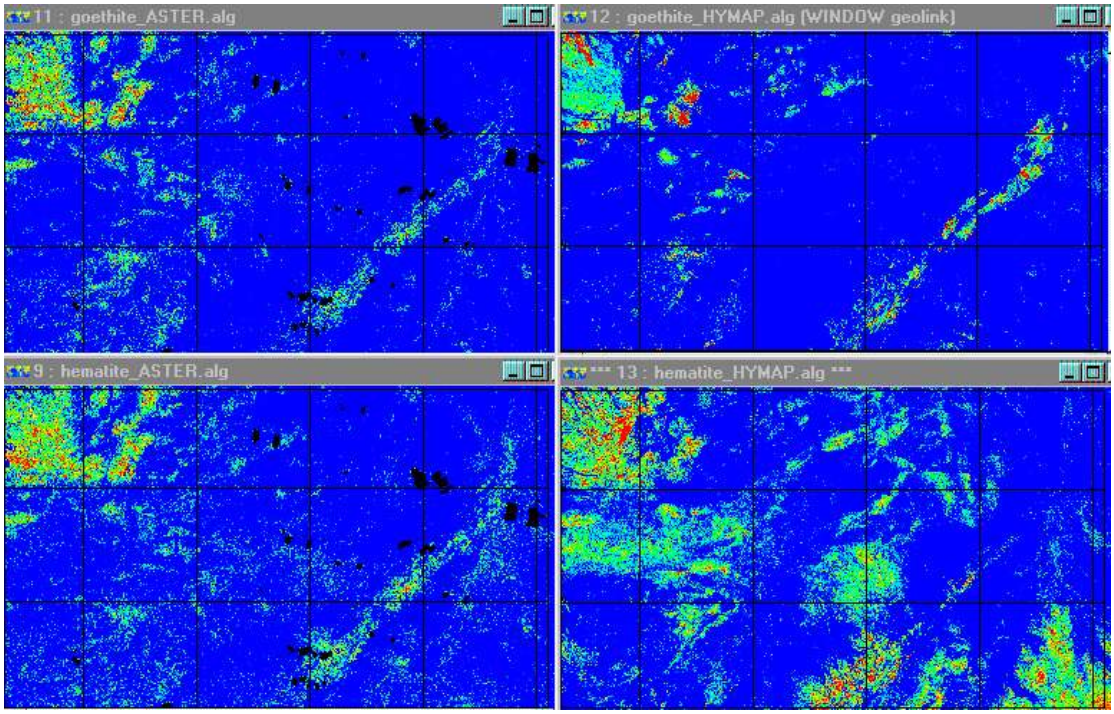

Figure 14. MTMF results for (top) goethite and (bottom) hematite - comparison of ASTER and HYMAP data.

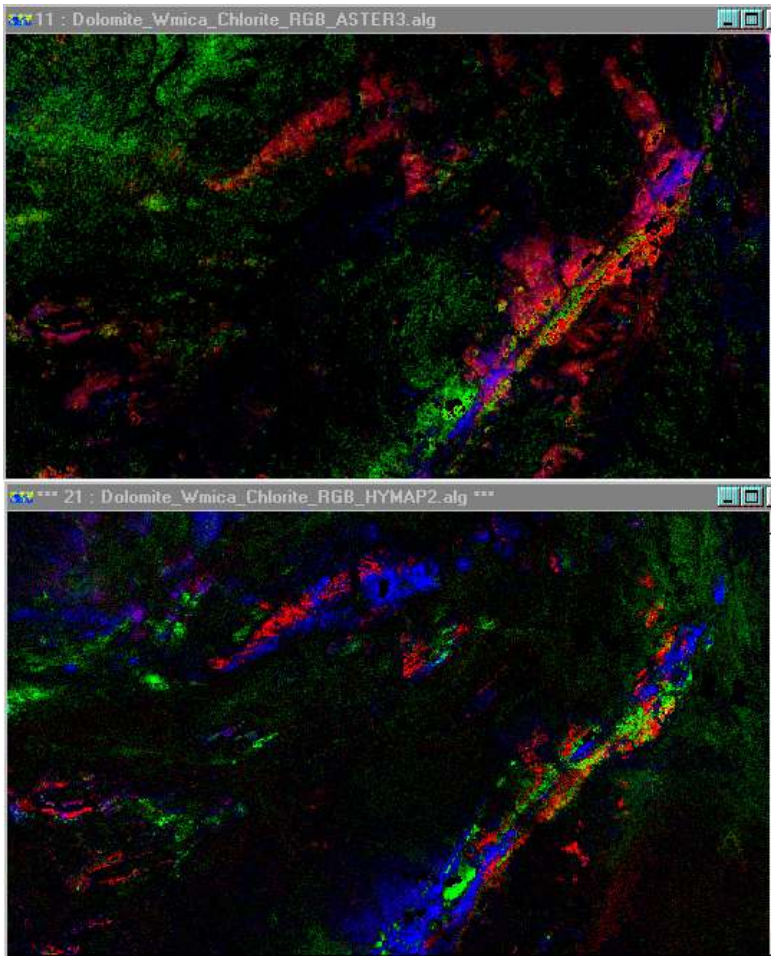

Figure 15. Colour composite of MTMF unmixed carbonate, white mica and Fe-chlorite as RGB for (top) ASTER and (bottom) HYMAP.

Three end-members are shown as a colour composite in Figure 15. The area contains a number of prospects associated with prophyllite, white mica and chlorite alteration. The ASTER data in this case failed to detect some hydrothermal chlorite and pyrophyllite (top-middle of image) but was effective in detecting hydrothermal white-mica in a number of locations.

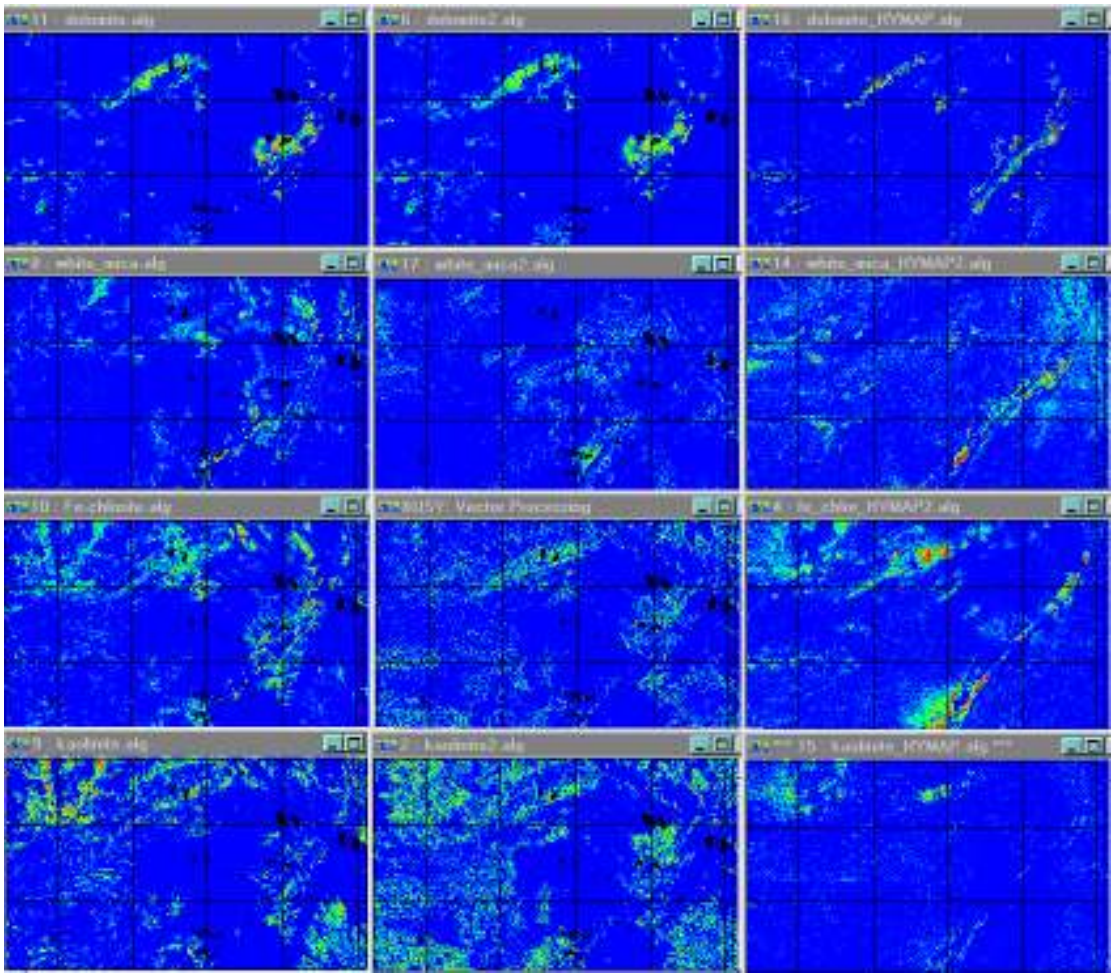

Figure 16. SAM results with a rainbow colour scale (red = low angle, i.e. a high match score) for dolomite, white mica, Fe-chlorite and kaolinite. The left column of images is results of analyzing ASTER bands 1-9, the middle column is processed from bands 5-9 and the last column is the HYMAP "ground truth" data.

3.1.7.2 Spectral Angle Mapper

Like MTMF, the Spectral Angle Mapper (SAM) is a method for comparing image spectra to individual spectra or a spectral library (Kruse *et al*., 1993a). Simply put the method maps the spectral angle between the target and reference spectra. The method was tested using both the ASTER VNIR-SWIR (bands 1-9) and just the SWIR level 2 reflectance data (bands 5-9). Figure 16 shows these SAM results for four minerals. Dolomite works quite well and is similar using both wavelength ranges as input. However the images for the other minerals, white mica, Fe-chlorite and kaolinite, are not working adequately and appear to be extremely sensitive to vegetation effects. In fact, the outline of the fireburn area (see Figure 2) is evident in the dolomite, chlorite

and kaolinite images. Although very noisy, the SWIR-derived chlorite image does detect the hydrothermal chlorite area in the middle-top of the image. Given that SAM is not an unmixing method, spectral angles will always be highly sensitive to vegetation and other materials in mixed pixels.

3.1.7.3 Ratios

Figure 17 (a-d) shows several ratios a compared with an ASTER colour composite image. Figure 17(A) is reasonably effective (although noisy) for mapping clay minerals, white mica and kaolinite. A multiple ratio using bands 6-9 is also quite effective at mapping carbonate combined with chlorite (Figure 17C) although the burnt area (blue in Figure 2B) outline can be seen. The ratio in Figure 17(D) was an attempt to separate calcite but this ratio is highly sensitive to dark vegetation. In general, though, ratios are prone to mixture problems including vegetation effects

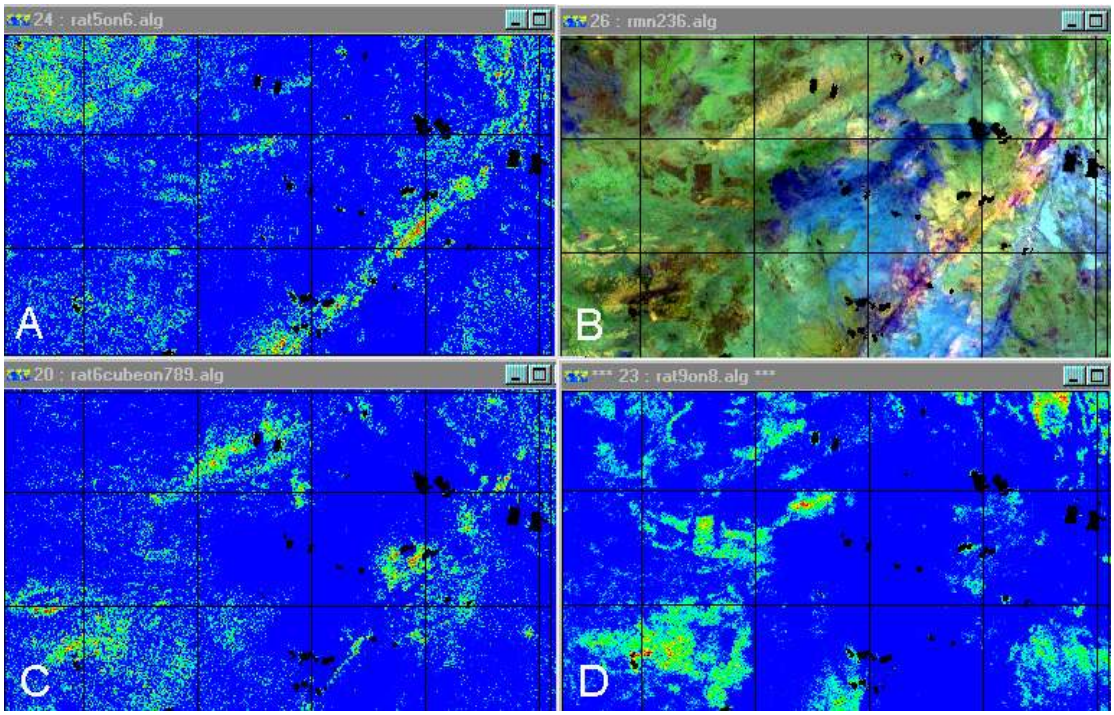

Figure 17 ASTER ratios. (A) a clay ratio – bands 5/6 (2.165/2.205) (B) composite of ASTER reflectance bands 1,3 and 6 as RGB respectively (C) a carbonate / chlorite ratio – bands $6^3/(7*8*9)$ and (D) a calcite ratio – bands 9/8.

3.1.7.4 Other methods – Comment

Log Residuals is suggested as potential analytical method (R. Hewson, GA ASTER processing course. March, 2001). This method was tested here and found to be largely ineffective largely due to vegetation / fireburn variations in the study area. Like SAM, methods that do not unmix minerals from vegetation effects will be prone to these problems. Linear unmixing is potentially extremely effective at achieving unmixing. This involves the inversion of a matrix of known spectral end-members (i.e. materials) that comprises a mixing model for a given pixel. This is essentially solving simultaneous equations where the unknowns are material abundances as proportions

of a pixel. The problem for linear unmixing is finding effective end-members to the mixing model and there may be many more scene components than bands.

3.1.7.5 Pixel purity index and N-Dimensional Visualizer

MNF bands are used as input to the Pixel Purity Index (PPI) routine in ENVI. PPI finds the most extreme pixels in the n-dimensional space of the image data by repeatedly projecting n-dimensional scatter plots onto a random unit vector (see ENVI tutorial notes). Firstly, bands 1-9 of the level 2 reflectance data were converted to MNF bands. A PPI image was obtained using this data and pixels above a certain threshold (Figure 18 - bottom-left) were imported into the N-D Visualiser (in this case about 1000 pixels). Figure 18 (top-left) shows the selection of pixel groups in the dimensional space of 3 of the MNF bands. These pixels were then exported as n-d classes to "region of interests" and their average spectra calculated from the image reflectance data (Figure 18, right). The brightest spectra again show the problem of the presence of the 2.165 feature, which is likely due to calibration problems (as discussed earlier). The n-D classes were used to generate Matched Filter images and the results of these allowed identification of the class spectra: (1) dark woody vegetation (mulga?), (2) green vegetation (3) dark areas (mainly Fe-oxides) (4) carbonates (5) vegetation related (burnt areas) and (6) burnt areas although slightly different. Not much success was achieved in the relatively limited time spent on this process. Better success may have been achieved using just the ASTER SWIR bands but this method can be a difficult and time-consuming way of hunting down end-members.

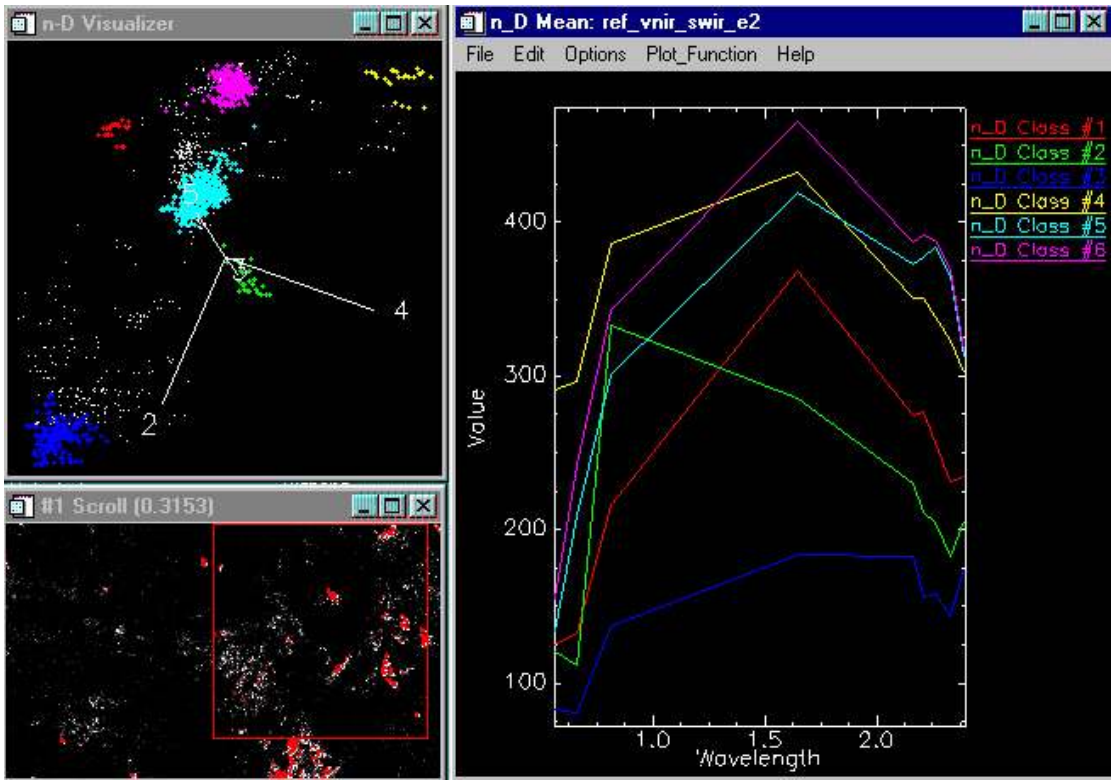

Figure 18. N-dimensional visualization selection of pure pixel classes in MNF space, (bottom-left) thresholding of these pixels from the pixel-purity image and (right) average spectra for the "visualized" classes.

3.1.8 Thermal infrared analysis

3.1.8.1 Mineral emmissivity spectra

As discussed earlier the ASTER thermal bands (bands 10-14) are derived from thermal emission from the surface (see section 2.2). The ASTER thermal IR data has 90 metre spatial resolution. Thermal radiance depends on both the temperature and spectral emissivity properties of the surface. For this study, the ASTER level 2 (Surface emissivity – Ast05) data was acquired as an on-demand product from the USGS. Figure 19 shows emissivity spectra of common minerals in the Indee area at laboratory and ASTER resolution.

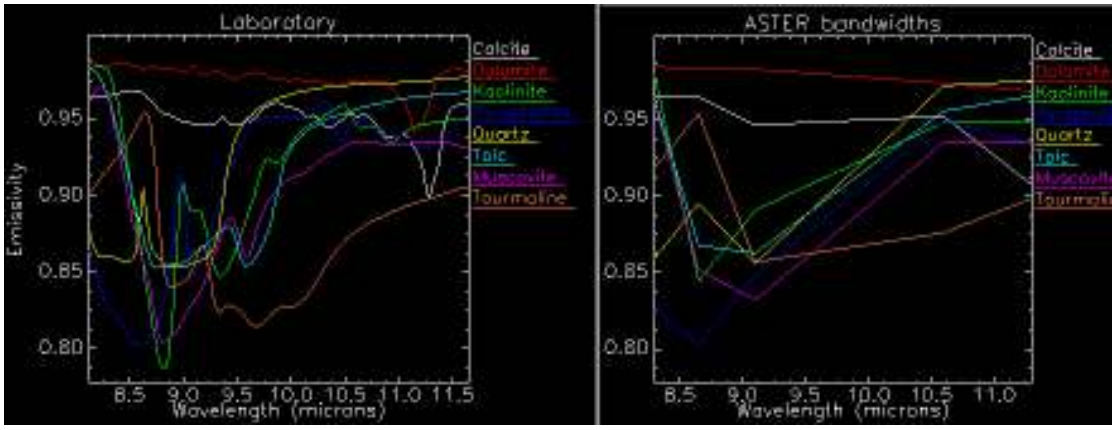

Figure 19. Emissivity spectra of minerals found in the Indee, Pilbara area for laboratory (left) and ASTER (right) resolution.

3.1.8.2 Results of the temperature / emissivity separation (TES) algorithm

The TES algorithm is described in detain above in section 2.2.3 and is designed to provide emissivity information free from the effects of temperature. Figure 20 shows the 5 TES bands as well as an image that represents temperature (bottom-right) and was generated by PC analysis of level 1B TIR data. Much higher temperature are observed in the fireburn area, due to lack of vegetation and surface. This effect appears to have been removed from the TES images indicating success of the algorithm. Bands 13 and 14 are very noisy and this perhaps should be dealt with prior to rectification of the data.

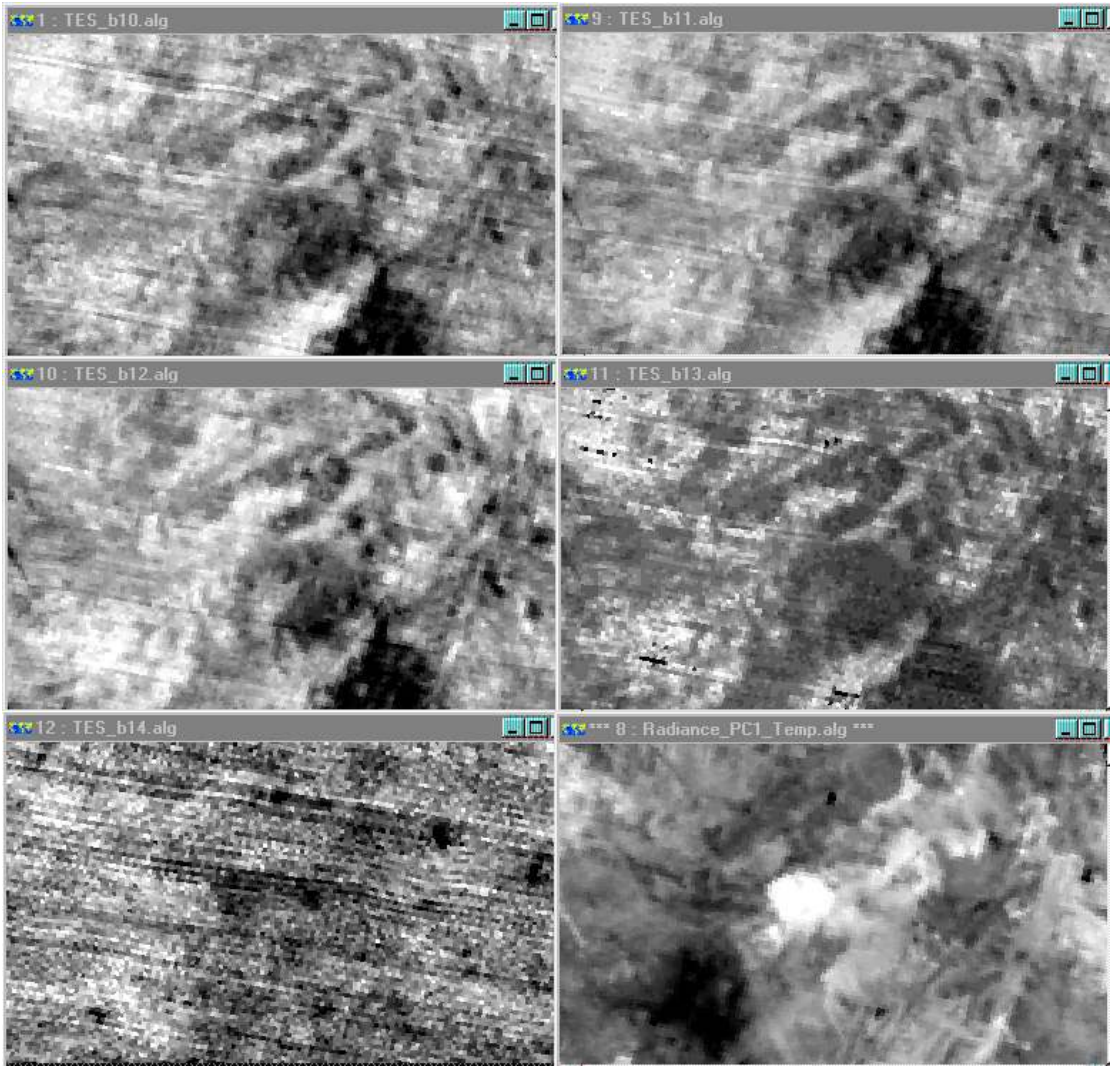

Figure 20. ASTER emissivity bands from the level 2 data for the Indee study area (12 x 7 km). The image at bottom-right is PC1 of level1b TIR data and represents temperature.

3.1.8.3 TIR mapping methods

A selection of processing methods are shown in Figure 21. Ratios designed by Ninomiya and Fu (2001) for silica (b11*b11/b10/b12), carbonate (b13/b14), basic degree index (b12/b13) were tested along with decorrelation stretch (see description in section 2.2.2) of TES and level 1B data. The ratios don't appear to be working at all and, similar to VNIR-SWIR ratios, are affected by vegetation. As expected, temperature effects are seen in the decorrelation stretch of radiance data (Figure 21, bottom-right). The best approach here is the decorrelation-stretch of TES data. Comparison with the geology image (Figure 21, top-left) shows that outcrop areas show as magenta to blue colour, with the intense white-mica alteration zone (bottom-middle of image) showing as blue. Red areas are sand soils but exposed by bush-fire. Light green areas correspond with green vegetation, which has a high emissivity.

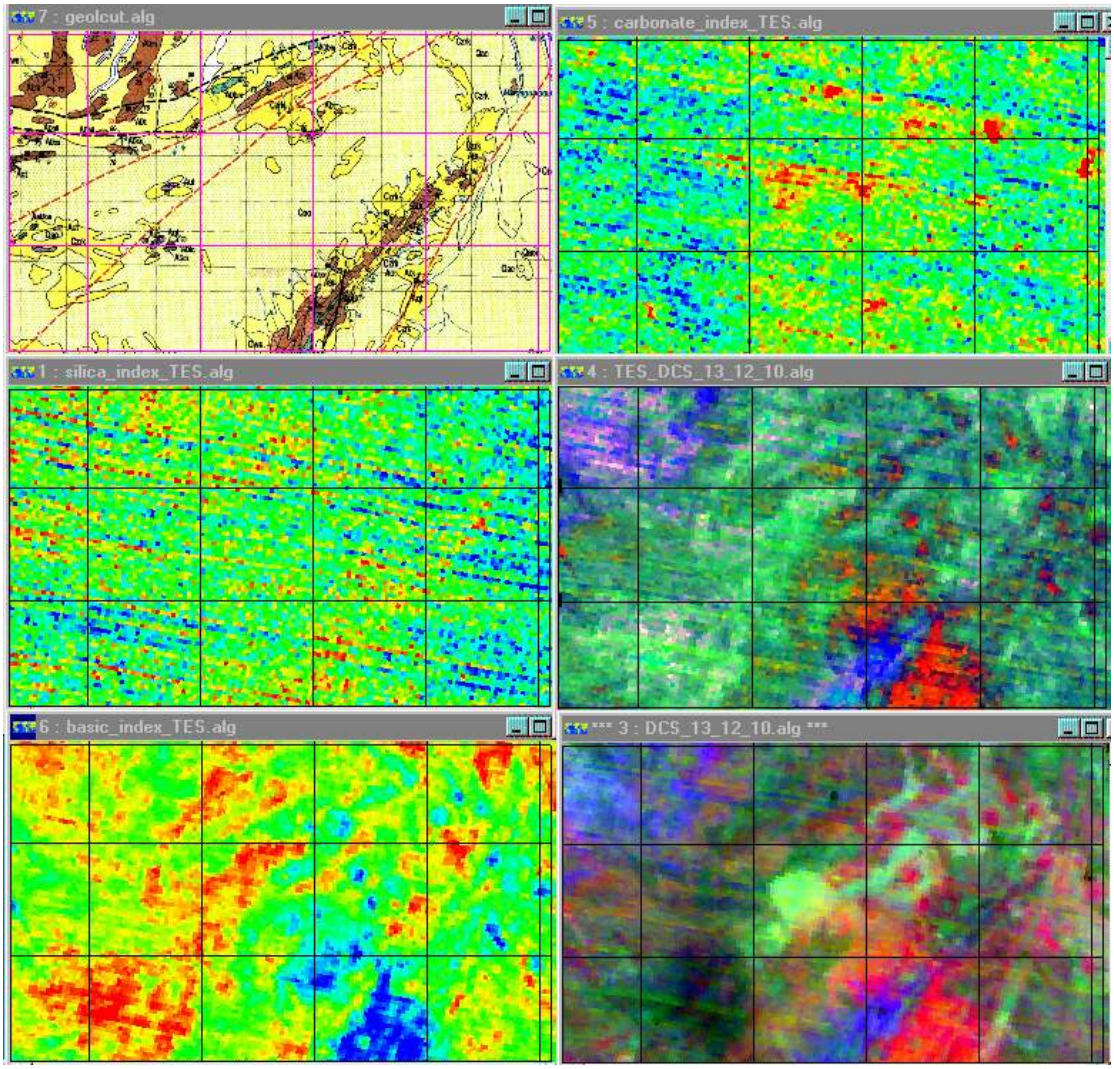

Figure 21. (Top-left) geology of the area – dark brown and green areas are Archaean bedrock, bright yellow is calcrete and pale yellow is sand, (left-middle) silica index (see text), (left-bottom) basic index, (right-top) carbonate index, (right-middle) Decorrelation stretch of TES bands 13,12 and 10 as RGB, (right-bottom) Decorrelation stretch of level 1B bands 13,12 and 10 as RGB.

3.2. Study site 2: Laverton, W.A.

3.2.1 Introduction / Geology

This work involves investigation of a single ASTER scene for the Laverton area (W.A). Level 2 reflectance data for bands 1 to 9 were provided by Geoscience Australia. Level 1B radiance data were also provided so that some analysis of thermal infrared (TIR) data could be performed.

The scene is centred on the southeast part of the Laverton 1:250,000 map sheet - on the adjoining area of the Laverton and Burtville 1:100,000 sheets. It includes the Laverton township, Granny Smith mine and Lake Carey. The Laverton 1:250,000 sheet lies within the Eastern Goldfields Province. Broadly, the study area consists of Archaean bedrock, Cainozoic laterite and Cainozoic colluvium, sandplains, sheetwash

and playa deposits (Gower, 1976; Stewart, 2001). The Archaean rocks comprise metamorphic (low to medium grade) volcanic and sedimentary rocks (greenstones) intruded by granitoids. Most outcrops are deeply weathered making field identification difficult (D. Champion, pers.com.). Resistant greenstones and laterites form hills and ridges, the most resistant are the chert or banded-iron formation (BIF) (Stewart, 2001). For ease of presentation, a study area was clipped inside the parallelogram of the raw ASTER scene to form a rectangle and the equivalent area of the geological map is shown in Figure 22 below

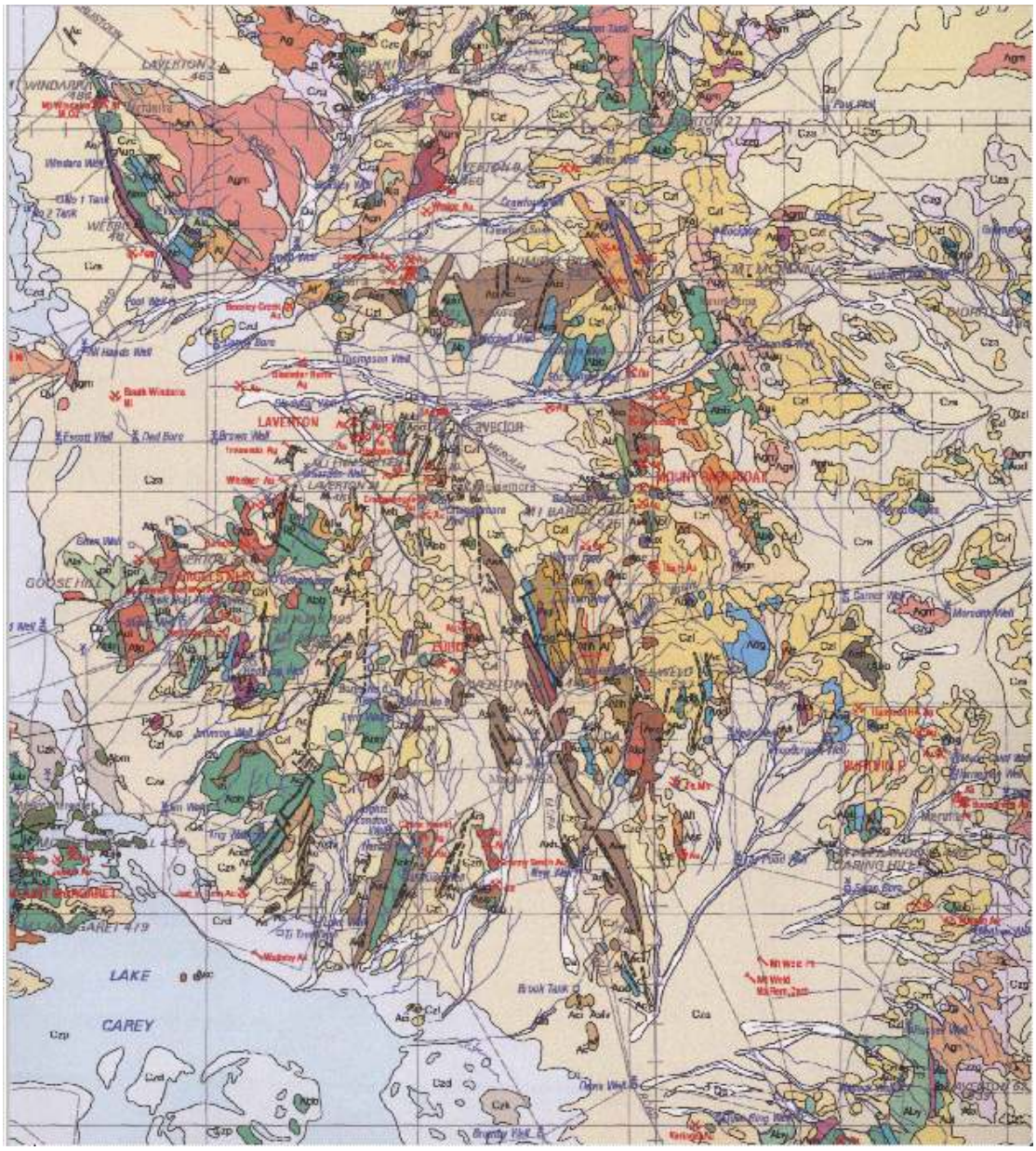

Figure 22. Geological map of the Laverton ASTER study area (from Stewart, 2001)

Minerals associated with the various rock-types that can be detected with remote sensing were noted (Stewart, 2001). For mafic and ultramafic rocks, these minerals include amphiboles actinolite and hornblende, serpentine (Aux, Aus), talc (Aut) together with secondary talc, chlorite, epidote and carbonate. Intermediate felsic rocks also contain amphibole (Afia, Afih) and more acid felsic rocks contain biotite (Af)

and muscovite (Afs, Aft). Illite and kaolinite would probably be expected as weathering products from felsic rocks. This would be similar for granitoids where primary minerals include muscovite, biotite and chlorite. Syenite (Ags) and tonalite (Agt) also contain significant amphibole. Illite (Ash) and muscovite (Ass) are found in sediments while goethite, hematite, calcite and gypsum are found in cainozoic deposits.

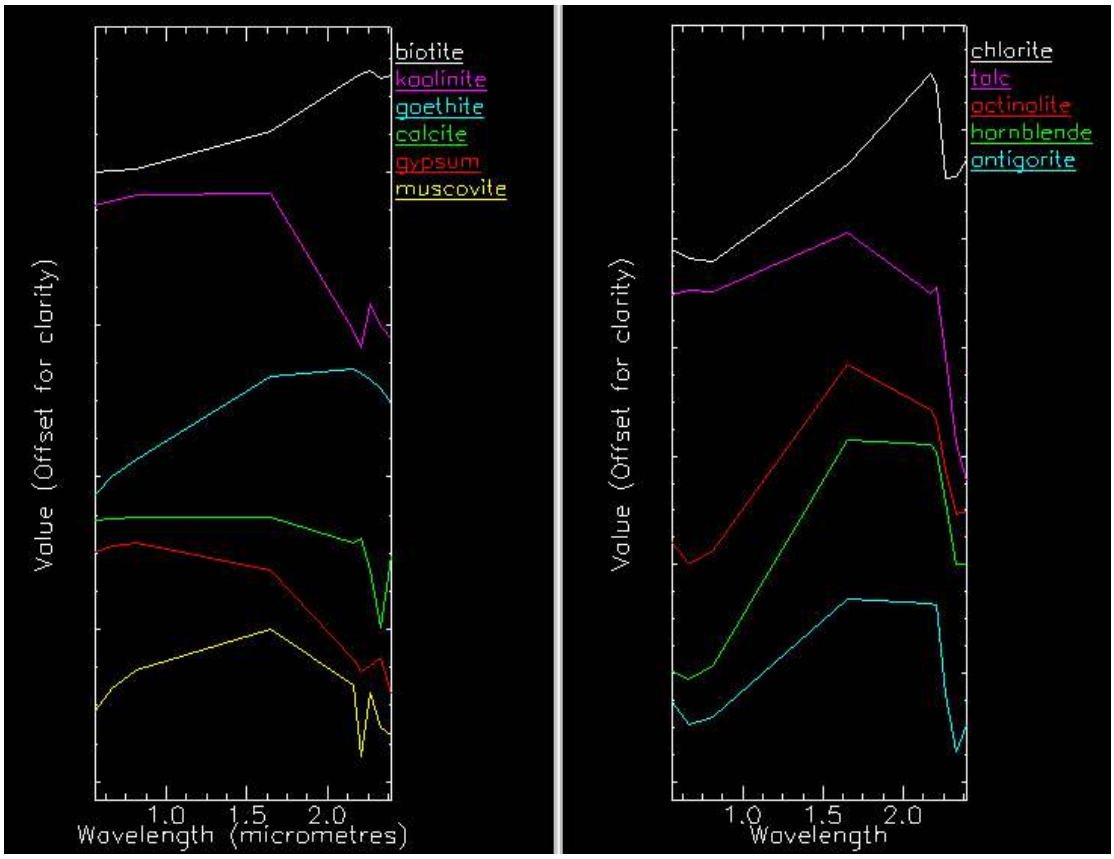

Figure 23. Laboratory spectra resampled to ASTER wavelengths for minerals likely to be present in the Laverton area.

Figure 23 shows ASTER spectra for the minerals mentioned above. The use of these spectra as end-members for mineral mapping yields poor results. This means that despite correction to reflectance, the conversion is not accurate enough for matching of ASTER image data to laboratory data. Nevertheless, these spectra should be useful for interpreting ASTER pixel spectra. Certainly there is a challenge for identifying relatively pure pixels where no hyperspectral data exists.

3.2.2 ASTER preprocessing

The following preprocessing steps were undertaken on the ASTER data:

1) Image to Map Registration

A scanned and registered version of the 1:250,000 geology map was used as the registration base for the ASTER scene. A total of 23 control points were selected mainly from road intersections and creeks. Of these, 6 points had large residual errors and were deleted with a resulting average RMS error of about 2.5 (max 5.9).

Although the spatial accuracy of the 1:250,000 map may not be adequate for mapping from imagery, it was considered accurate enough for the demonstration work here, as later examples will show. Some workers have claimed that the ASTER data has relatively good spatial accuracy when imported into ENVI and system parameters are entered (R. Hewson, K. Pfitzner, pers. comm.). This needs to be properly investigated.

2) Band 9 reflectance correction.

As mentioned in the Pilbara section (3.1.6), the level 2 reflectance data has a clear problem in band 9. In the Pilbara case study, a multiplying conversion factor was found by the use of field spectra. The same factor was used to correct the Laverton data since it was assumed that average reflectance will be similar for both semi-arid regions.

3) Cloud identification and masking

Cloud areas were visually identified in VNIR data (see Figure 24 – a VNIR composite image) and regions of interest (ROI's) were drawn to characterize both cloud tops and cloud shadows. As with the pilbara study (see section 3.1.2), signatures from reflective bands (1-9) were collected and matched filtering was used to identify cloud affected areas. As with the Pilbara study, cloud shadows were best identified with all 9 bands whereas the cloud-tops were distinguished more easily from bright surfaces using only the SWIR bands (bands 4-9). These images were then used to create a cloud mask.

3.2.3.Vegetation

The region has a semi-arid climate. Vegetation tends to form associations with bedrock and regolith geology. Typically low woodland with mulga occurs on bedrock and laterite areas (Stewart, 2001). Mallee, spinifex and marble gum occur on sandplains while mulga and spinifex are found on gypsiferous dunes and small playas. Vegetation features can be seen on the colour composite in Figure 24 showing the same area as the above geological map. Green vegetation areas show as red due to high NIR leaf reflectance.

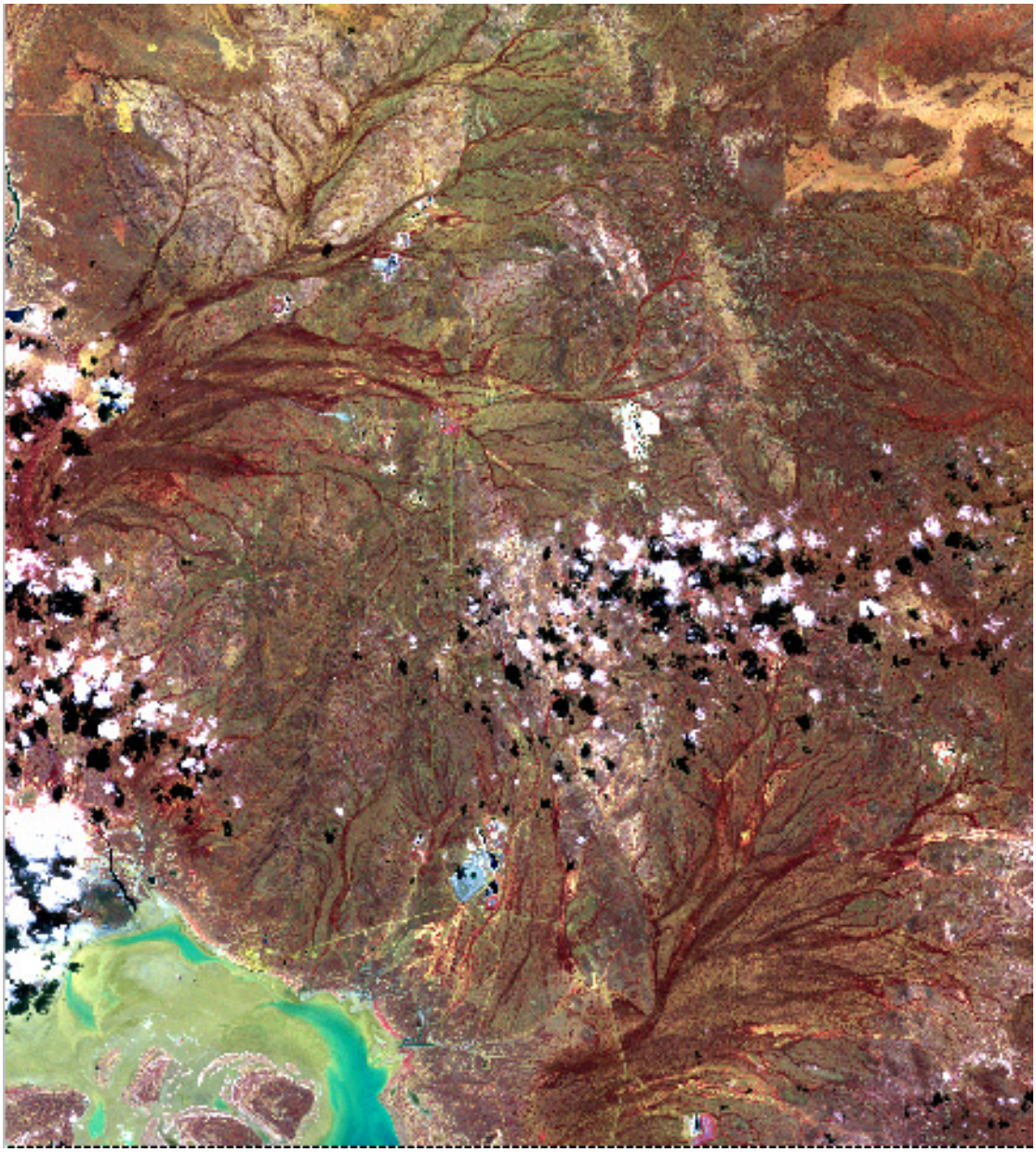

Figure 24. Colour composite of ASTER bands 3,2 and 1 as RGB respectively. The area is 49 x 54 km.

3.2.4 Finding scene end-members

As discussed in the work on the Indee, Pilbara area, a desired approach for scene analysis is to find image end-members and then use these to characterize materials. For the Laverton work, three approaches were tested:

1) average spectra for regions of interests associated with various bedrock and regolith types
2) thresholding of Minimum Noise Fraction (MNF) images
3) the use of the Pixel Purity index (PPI)

3.2.5 ASTER spectral signatures for rocktypes

Regions of interest were selected for various rock-types and regolith units by digital comparison of the geological map and and Principal Component Analysis (PCA) of the SWIR bands. An example of this is shown in Figure 25

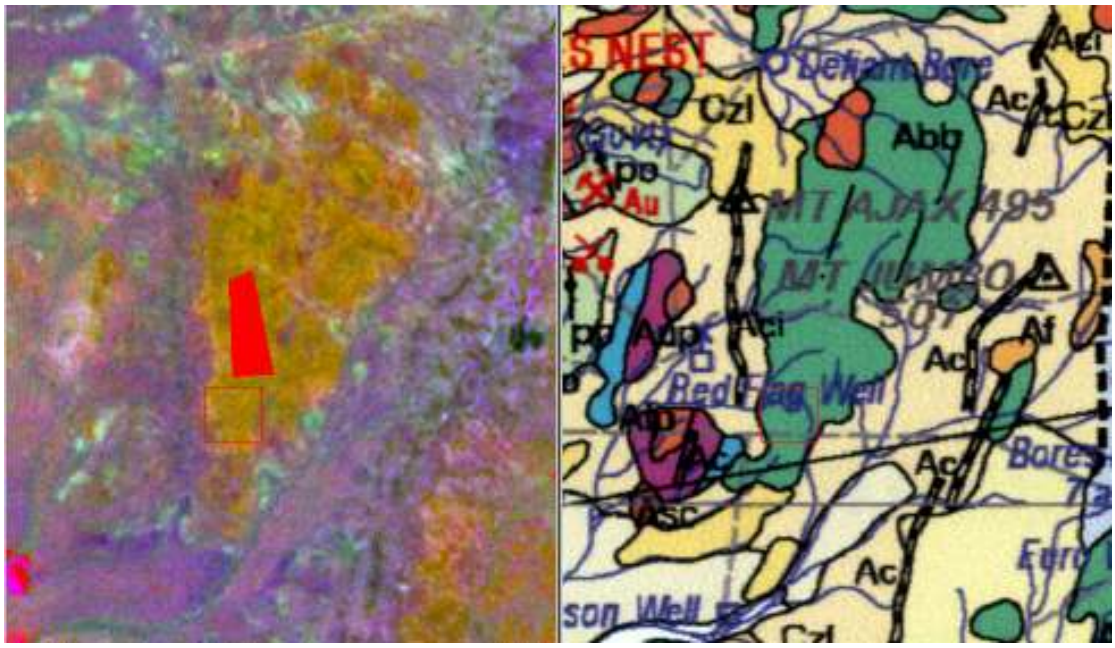

Figure 25. Selection of a region of interest for the metabasalt unit (Abb) for averaging of spectral signatures. The image at left is PC 1,2 and 3 of ASTER SWIR bands (4-9) displayed as RGB respectively.

The PC image represents most of the spectral variation in the 6 SWIR spectral bands. By comparison also with a VNIR image (e.g. bands 3,2 and 1 combined as RGB), it was possible to select sparsely vegetated and uniform spectral areas that were likely to be largely influenced by the mapped rock unit. Spectral signatures obtained in this way are shown in Figures 26 and 27.

ASTER vegetation signatures (Figure 26, left) appear to correlate well with laboratory readings indicating that the reflectance data is reasonable in terms of the accuracy of calibration. Of interest is what appears to be a small feature in the 2.165 band (band 5) which appears to be an effect of the broad 1.9 μm feature in green vegetation and the 2.1 cellulose feature in dry vegetation. These features could be very important for interpreting ASTER data where there are variable vegetation effects.

In general, granitoids and felsic rocks (Figure 26, right) are characterized by the presence of the 2.2 μm feature (band 6) and higher reflectance at 2.26 μm (band 7). This indicates higher concentrations of muscovite or illite in these rocks with the most abundant muscovite present in the Granny Smith mine wallrock and the Barnicoat mine tailings. Curiously there is significant 2.165 (band 5) absorption in most of these rocks and this is very difficult to explain because there are no AlOH minerals such as pyrophyllite or alunite recorded in the area (Stewart, 2001). Also the feature is not obvious in vegetation and many of the Cainozoic deposits. The graphs in Figures 26 and 27 are relative reflectance, but it is apparent that the higher the reflectance for the general SWIR spectrum, the 2.165 absorption is more intense. This feature appears

therefore to be a calibration problem particularly affecting the high range of band 5 and certainly needs further investigation.

The mafic and ultramafic units (Figure 27, right) generally lack the 2.2 feature (although seen in peridotite and pyroxenite possibly due to chlorite weathering to kaolinite), has lower band 7 (2.26 μm) reflectance. These spectra are dominated as expected by the presence of amphibole (i.e. actinolite and hornblende) (see Figure 23) although band 7 has higher reflectance and band 9 (2.395 μm) has lower reflectance than expected. Again the more reflective and more felsic units (Afia and Afih) have the strongest 2.165 μm absorption. There is no sign of variations due to talc, serpentine or chlorite, which should mainly show up as variations in band 9. Unfortunately there is no accurate ground information on mineral concentrations that could help identify these end-members spectrally.

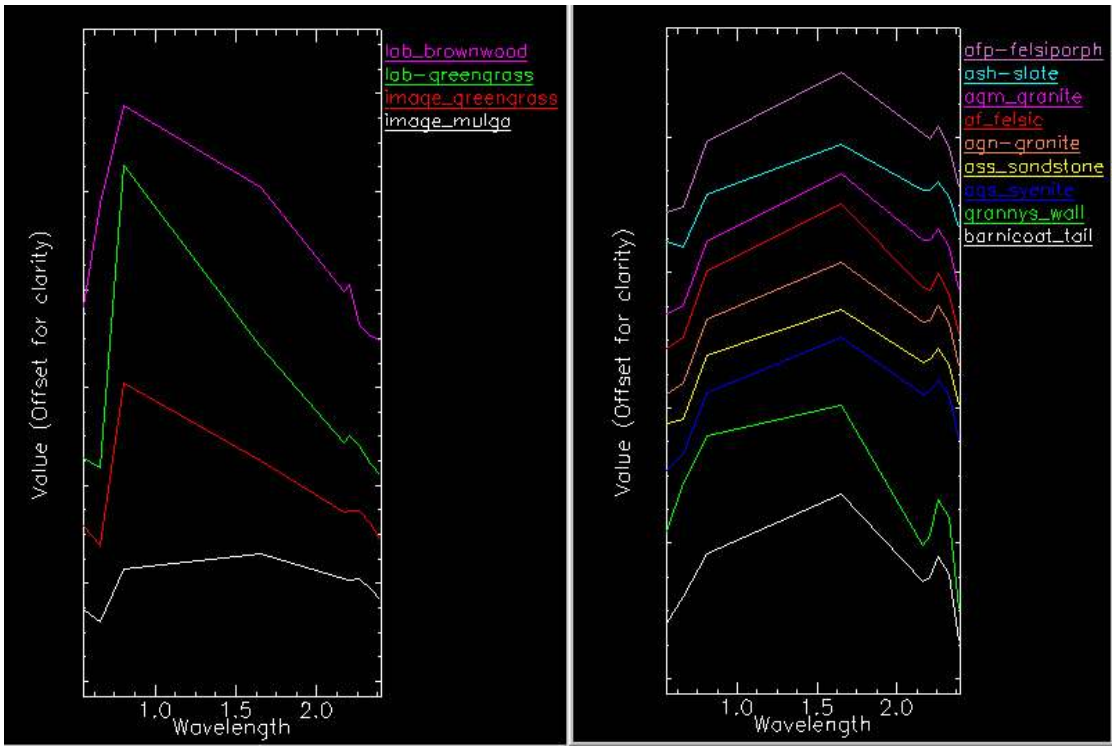

Figure 26. Average ASTER image spectra for (left) vegetation compared with laboratory data and (right) granitoids, felsic and sedimentary rocks.

Cainozoic regolith units (Figure 27, right) have a range of signatures. To enhance the point of potential calibration problems again, the highest SWIR reflectors (Czs – burnt, Czd and calcretes) all have a significant feature at 2.165 μm. A comparison of the unburnt and burnt sandplain (Czs) shows that the 0.66 μm chlorophyll absorption is present for unburnt while the 2.165 feature is not. The SWIR bands appear to show kaolinite as expected but the burnt Czs spectrum is showing the 2.165 μm feature that is not expected and unlikely to be present in the field.

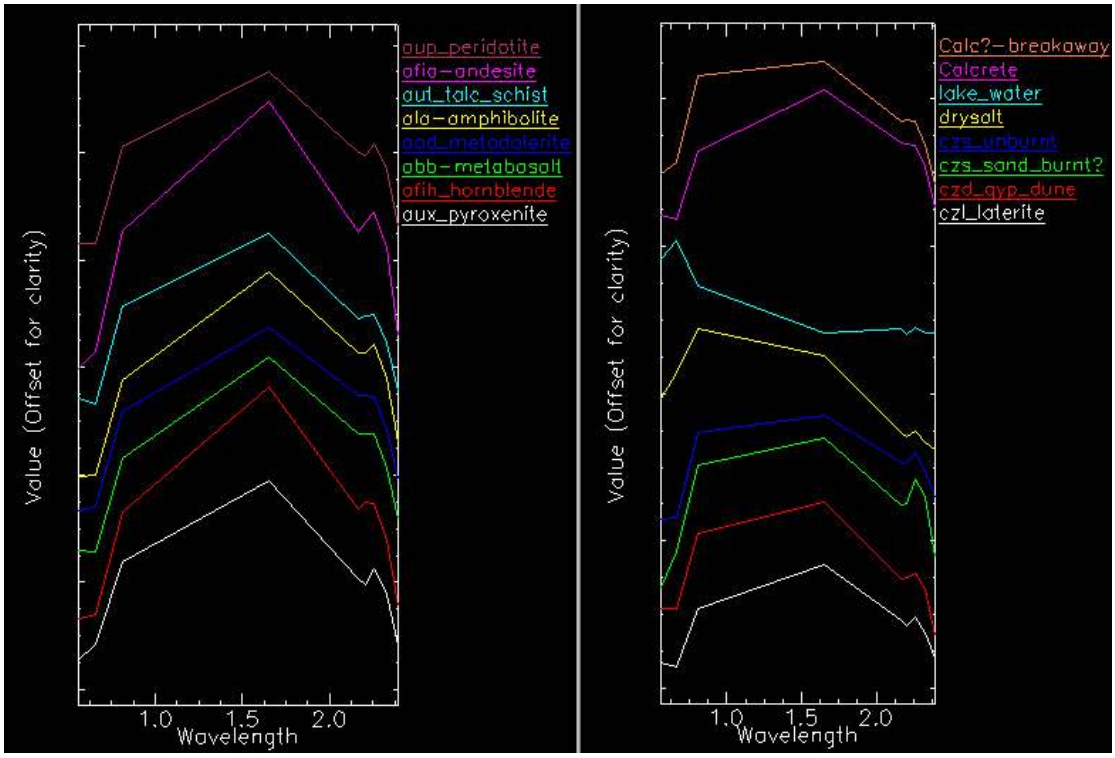

Figure 27. Average ASTER spectra for (left) mafic and ultramafic rock-units and (right) Cainozoic deposits.

3.2.6 Level 2 Recalibration of Level 1B data due to Problems with Level 2 data.

In the light of problems observed in ASTER Level 2 reflectance product, it was decided to test approach of converting level 1B data using a gain correction similar to the reflectance-mean normalization (RMN) method described in the Pilbara section where field spectral measurements were used to find conversion gains). The Laverton level 1B data was converted by first subtracting scene minimum values using gains that would equalize the spectra of clouds to those in the Pilbara RMN data. This processing was done in ENVI using the "spectral math" function. Figure 28 shows a comparison of level 2 reflectance and RMN signatures for cloud-tops and cloud-shadows. There is clearly a problem with the shape (and the 2.165 μm absorption) of the top-of-cloud spectrum in the level 2 ASTER SWIR data which is similar to the bright ground signatures in Figures 26 and 27. In contrast, the cloud spectrum resulting from image-reflectance calibration based on ground spectra (RMN) is fairly smooth. This is likely to be much closer to the truth given the lack of individual water absorption bands in the SWIR. The cloud shadow spectrum is also smoother for the RMN method although the apparent features in the SWIR may be noise given that there would be low signal in shadows and the differences are based on a variation of only 4 DNs.

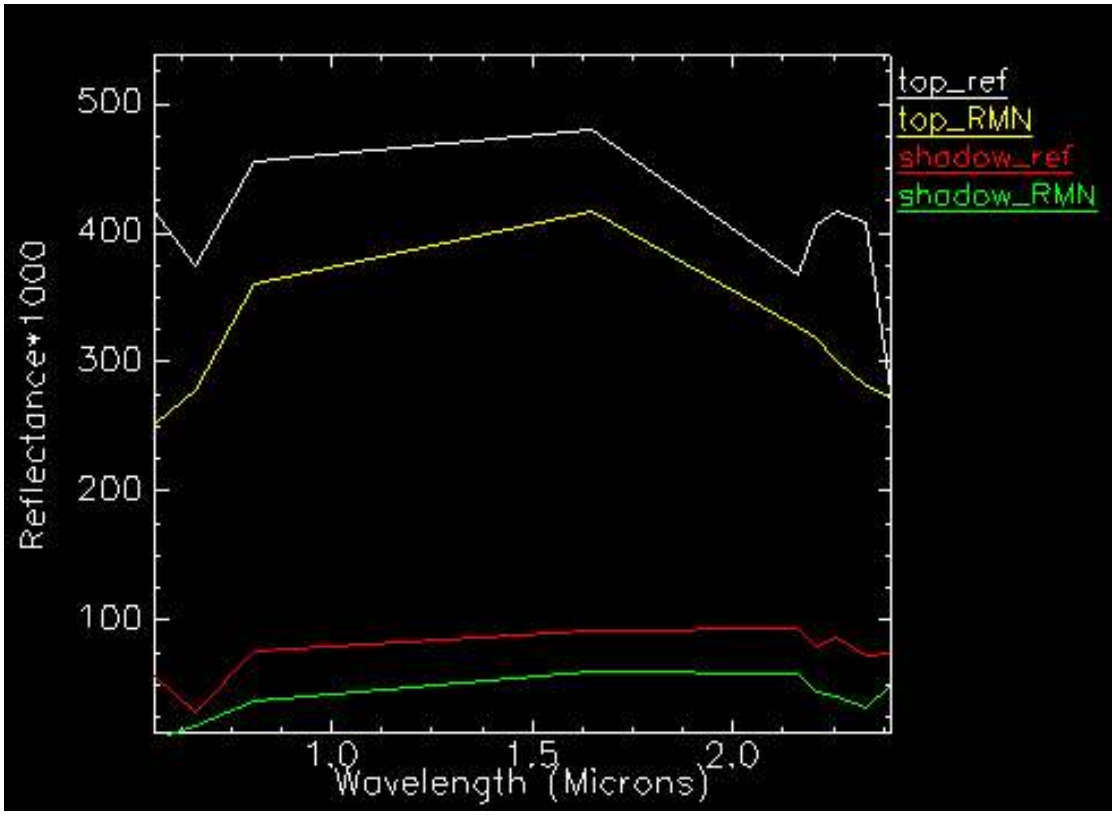

Figure 28. Comparison of cloud top and shadow signatures for ASTER level 2 reflectance data (ref) and reflectance derived by calibrating on cloud-tops (RMN).

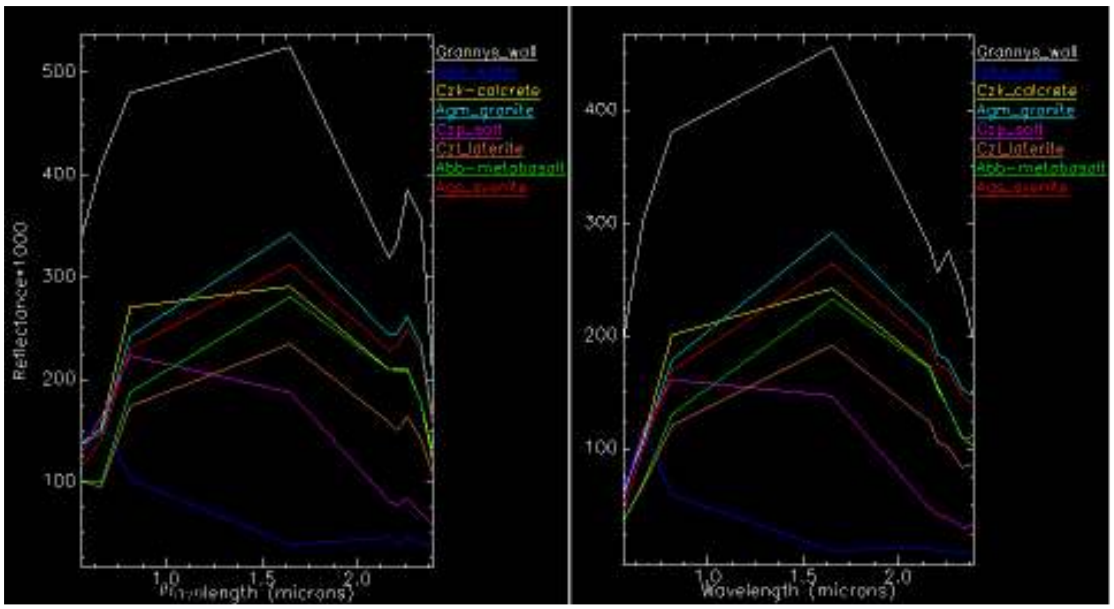

Figure 29. A comparison of rock-type signatures for (Left) ASTER level 2 reflectance data and (Right) reflectance derived by calibrating on cloud-tops (RMN).

Geological end-members for the same "regions of interest" shown in Figures 26 and 27 were recalculated from the RMN converted Level1b data. A comparison of the two reflectance-conversion methods for some of these units is presented in Figure 29. The large 2.165 μm feature in the brighter spectra of the level 2 reflectance (left) is now

not present at all in any of the spectra. A slight 2.33 μm (band 8) feature is present and was expected for the basic rock (Abb) due to amphibole and calcrete (Czk) due to calcite (see Figure 23). A small feature is there for the granitoids (Agm, Ags) due possibly to biotite (?) and in laterite (Czl) possibly due to clay, although these explanations are difficult to verify without measurements on field specimens. At least the comparison of image to laboratory spectra now makes some kind of sense (cf. Figure 23).

3.2.7 ASTER analysis for geological components

3.2.7.1 Matched Filtering

Rock-type and regolith-type spectra were used to generate Matched Filter (MF) images. Figure 30 is an example combining the use of averaged spectra for syenite (Ags, red), granite (Agm, green) and amphibolite (Ala, blue) and effectively shows the composition of rock-types is the area. The syenite and granite signatures are very similar (see Figure 26, right) but the subtle difference is enough to discriminate the syenite unit at A. Interestingly, this image shows a variation of composition between basic units at B and C. These two units are mapped as different units in the earlier version of the Laverton map (Gower, 1976) but not in the 2nd edition (Stewart, 2001).

3.2.7.2 Minimum Noise Fraction (MNF) image thresholding

Since the method described above collects average rock-type signatures for regions, the end-members are unlikely to represent anywhere near pure mineral spectra, also containing vegetation. As such, these end-members may not be optimum or extreme enough to produce the best rock-type or mineral mapping results. The MNF method is an orthogonal transformation in n-band dimensional space (like Principal Component Analysis – PCA), but orders the resulting MNF images based on spatial image-noise (Green et al. 1988). This method can sometimes find relatively extreme components in the data.

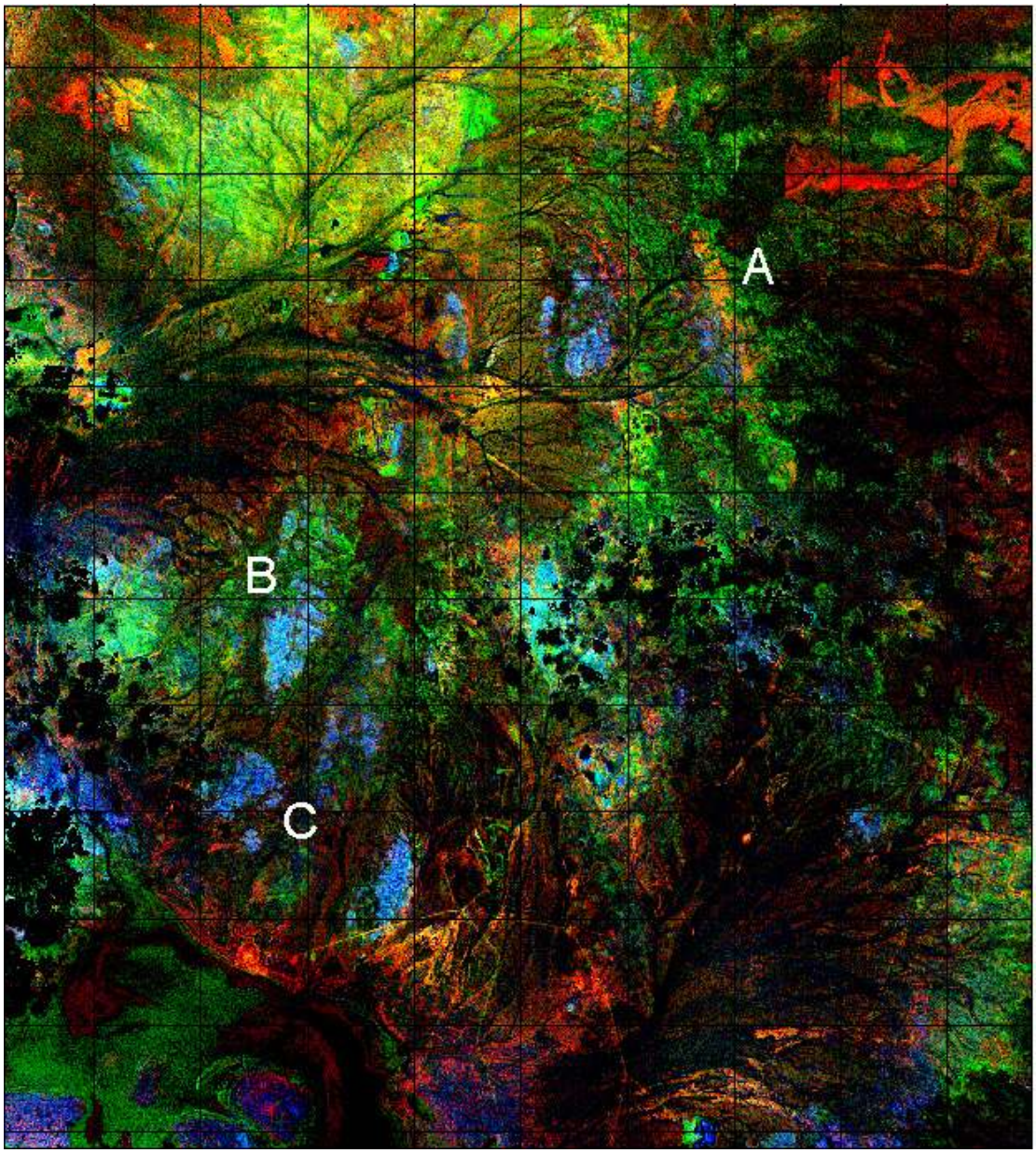

Figure 30. Matched Filter scores for rock-type averaged signatures, Ags syenite, Agm granite and Ala amphibolite as RGB respectively (see rock-types data set on accompanying CD-Rom).

For this area, the 6 SWIR bands were processed to produce MNF data (statistics were collected first for a large cloud free region). MNF bands 2 and 3 were effective at mapping amphibole and laterite respectively and these images were used to collect signatures for these materials, which in turn were used to generate MTMF abundance data. It was thought that this should produce better results than using the MNF data, since the mixing vector (particularly the low abundance end-point) should be better defined. Figure 31 shows the whole-area results for these end-members (c.f. geology in Figure 22). High MTMF infeasibilty scores have been masked from the laterite image (left) which included exposed mine areas and dry evaporites in Lake Carey – this masking may not be totally effective but generally the laterite areas are close to those that have been mapped (Stewart, 2001). The amphibole image is also effective

and maps out basic units in the area. Figures 32 and 33 show a more detailed comparison between the laterite and amphibole images and geology.

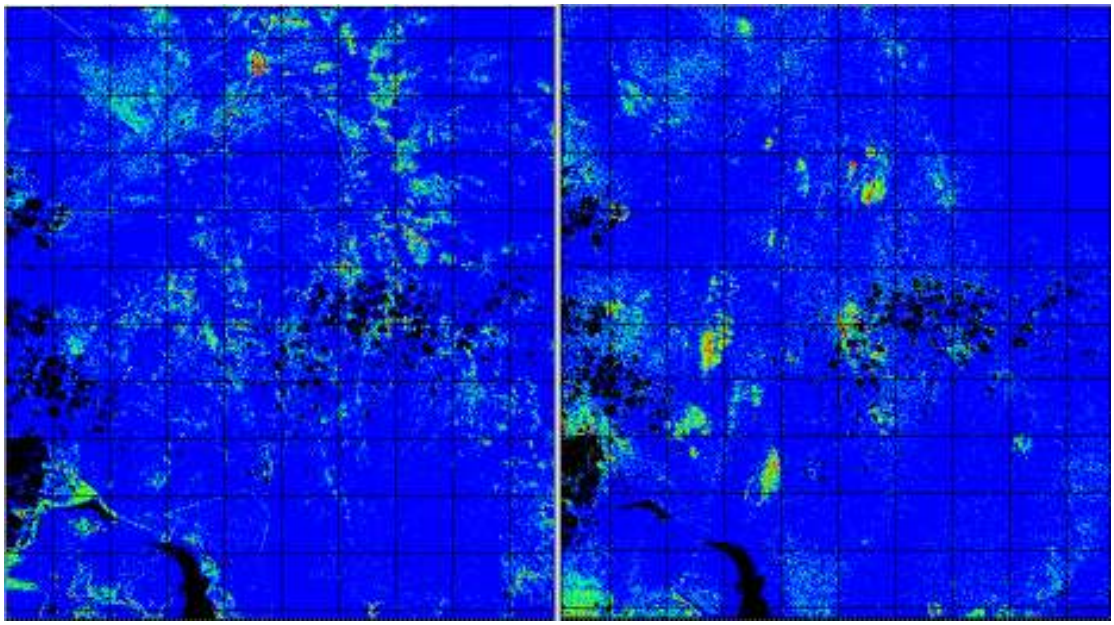

Figure 31. MTMF mapping of laterite (left) and amphibole (right) using signatures derived from MNF processing. The area is 49 x 54 kilometers, grid cells are 5 km (see laterite and amphibole data on CD-ROM).

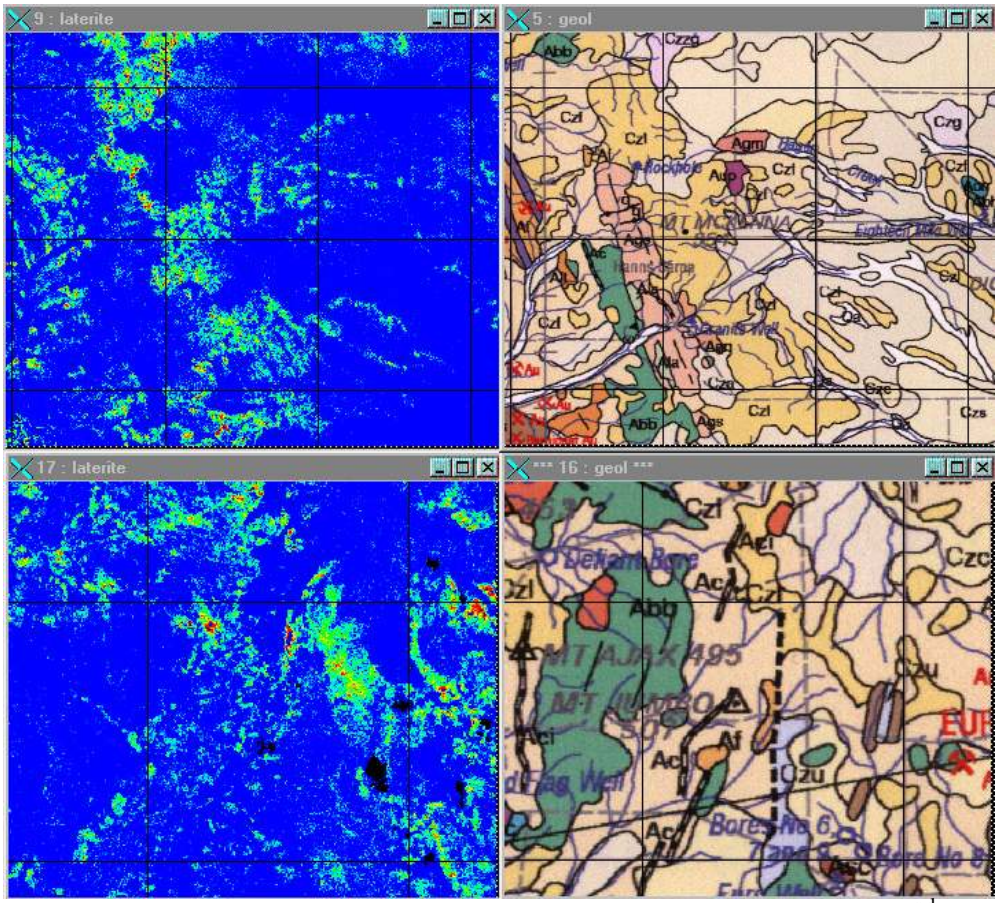

Figure 32. Zoomed-in areas comparing the MTMF laterite image with the 2nd edition geology (Stewart, 2001). Grid cells are 5km.

Figure 32 shows the comparison of laterite derived by MTMF for localised areas. The image at top shows a good match between the image and the mapping although the image suggests that the mapping boundaries are generous through simplification at this scale. The bottom image from further south suggests that laterite can be dispersed in nature and difficult to map accurately. In this way, ASTER data can provide more accurate representation of laterites.

A zoomed-in area of the amphibole image (Figure 33) shows that for some areas, the image data and the mapping do not match. The basic units in this small area (6 x 6 km) are a combination of metadolerite (Aod) and metabasalt (Abb). A basic unit is suggested by the ASTER data in the top part of the image where sandstone (Ass) has been mapped. Interestingly, metabasalt has been mapped previously in the 1st edition mapping (Gower, 1976) at precisely where the ASTER data indicates basic geology. The fact that correctly mapped geology has been wrongly re-mapped cannot be explained, but it serves to demonstrate the utility of remote sensing.

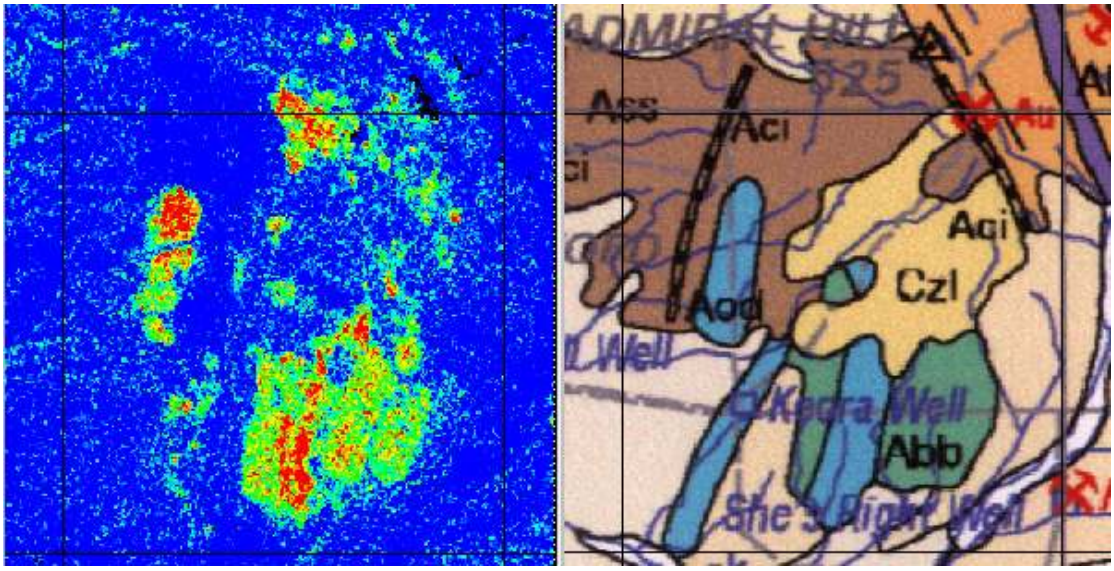

Figure 33. A zoomed-in area of the amphibole MTMF image demonstrating errors in the 2nd edition geological mapping. The area is 6 x 6 km.

3.2.7.3 Pixel Purity index (PPI) and N-Dimensional Visualizer in ENVI

MNF bands are used as input to the Pixel Purity Index (PPI) routine in ENVI. PPI finds the most extreme pixels in the n-dimensional space of the image data by repeatedly projecting n-dimensional scatter plots onto a random unit vector (ENVI tutorial notes). Firstly, the RMN-corrected reflectance data was converted to MNF bands using SWIR bands only. A PPI image (Figure 34, bottom-left) was obtained using this data and pixels above a certain threshold were imported into N-D Visualiser (in this case about 1500 pixels). Figure 34 (top-left) shows the selection of pixel groups in the 3 dimensional space of the first 3 MNF bands. These pixels were then exported as n-d classes to "region of interests" and their average spectra calculated from the image reflectance data (Figure 34, right). Classes 1 and 7 were related to

cloud shadows and tops respectively and are not shown. These spectra are not easy to interpret or understand what they relate to on the ground. Many of the spectra show the AlOH feature at 2.2 μm with class 9 looking influenced by muscovite and classes 2 and 6 more kaolinitic. Classes 5 and 11 appear to be related to amphibole rich basic rocks. The spectra in Figure 34 were then used to generate Matched Filter images using the 6 SWIR bands only. Surprisingly the results were poor. The clay rich end-members produced similar results with poor discrimination between felsic rocks and laterite. Similarly the class 5 spectrum did not discriminate basic rocks as clearly as the rock-type or MNF end-members described above.

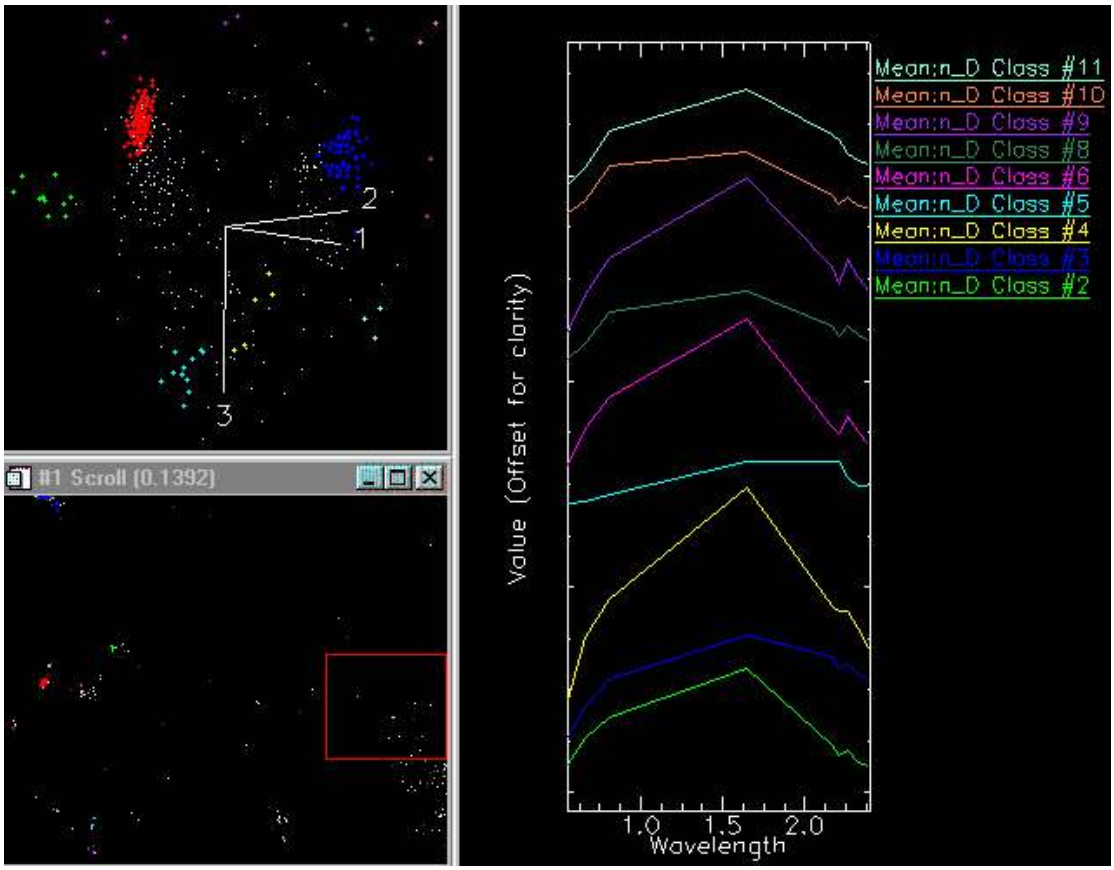

Figure 34. (Top-left) selection of pure pixel classes in n-D space (bottom-left) Colour classes on Pixel Purity image (right) average class RMN reflectance.

3.2.7.4 Ratios

In general, ratio enhancements provided poor results for the Laverton area. Figure 35 shows an example of a composite of 3 ratios designed to show clays, basic rock minerals and laterite. The image is noisy and is dominated by mixture effects particularly associated with vegetation.

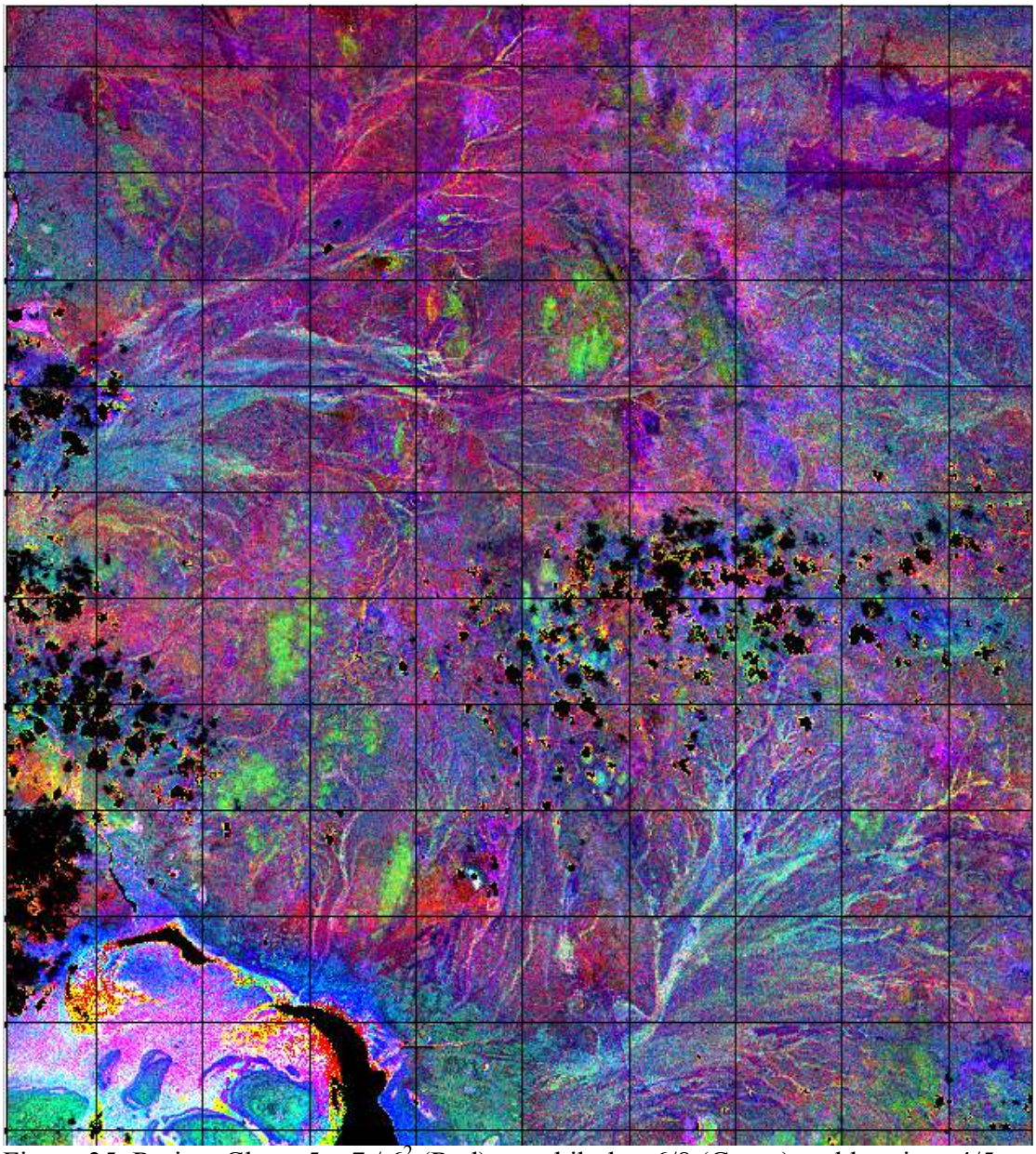

Figure 35. Ratios: Clay - 5 x 7 / 6^2 (Red), amphibole - 6/8 (Green) and laterite - 4/5 (Blue) for the Laverton study area.

3.2.8 Thermal infrared analysis

The thermal data used here are Level 1B since level 2 emissivity was not obtained for this project (unlike the Pilbara section work). A decorrelation stretch of bands 13, 12 and 10 (Figure 36) shows useful information about the geology although, compared with the VNIR-SWIR data, the TIR data is coarse and noisy. Red areas show exposed sandy soils on quartz-rich units and sand-plains due to the low emissivity of quartz in bands 10 and 12 (see Figure 19). Vegetation appears in this enhancement as light green colours and this is similar to the Indee study area. Clearly vegetation has a strong masking effect. Basic and ultramafic rocks generally show as cyan to blue respectively. Curiously blue areas also occur on the granite at top-left of the image.

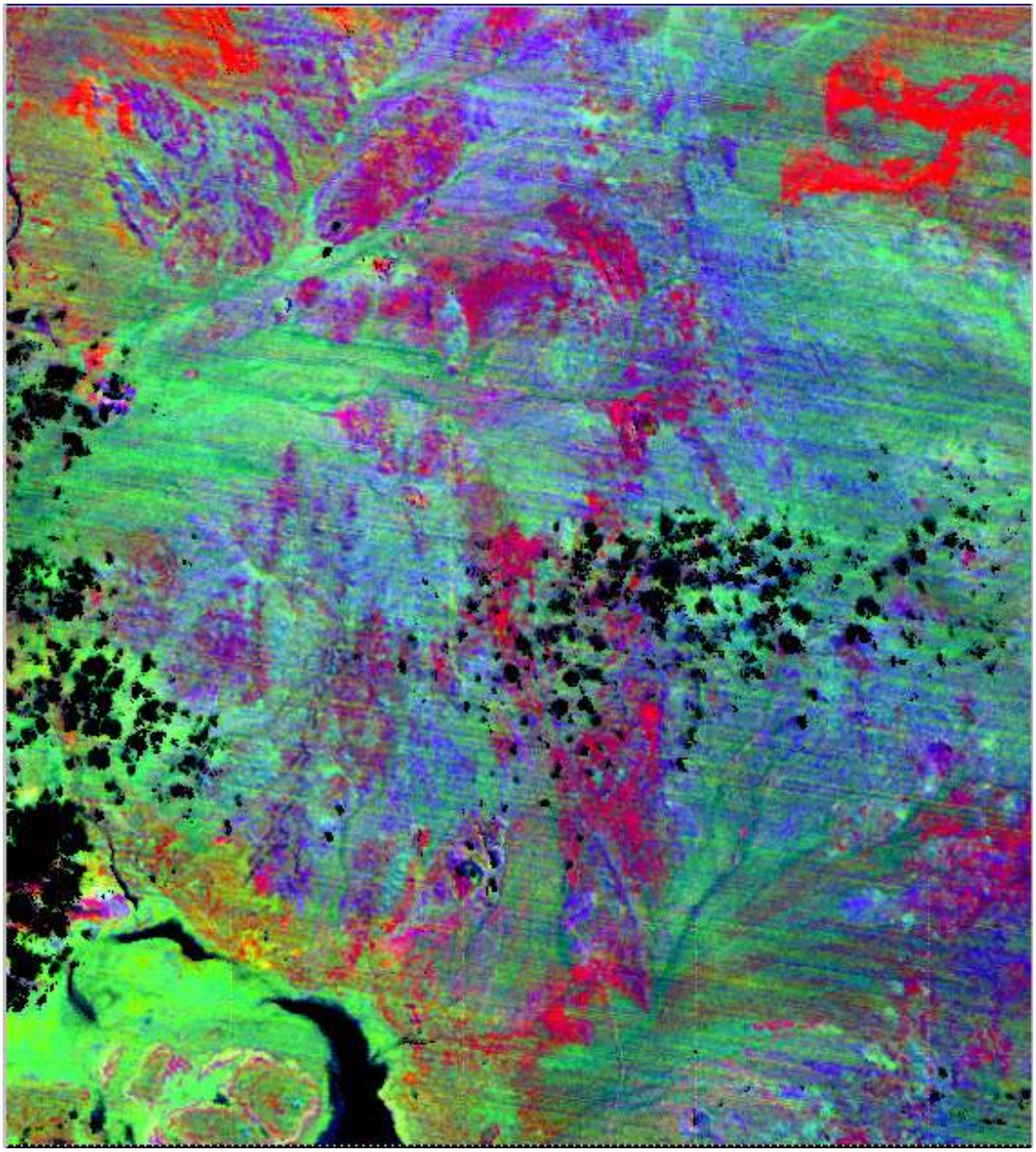

Figure 36. Decorrelation stretch of level 1B radiance bands 13, 12 and 10 as RGB respectively.

Figure 37 is a zoomed in area showing an area of sandstone (Ass), quartz-feldspar schist (Afs), metabasalt (Abb) and metadolerite (Aod). The quartz-rich units are clearly discernable as red colours but also so are areas of sandy colluvium derived from these units. A quartz rich component can be seen in the laterite area and these aspects are clearly important for regolith mapping. The basic units show as a cyan colour but are often difficult to differentiate from surrounding vegetated areas.

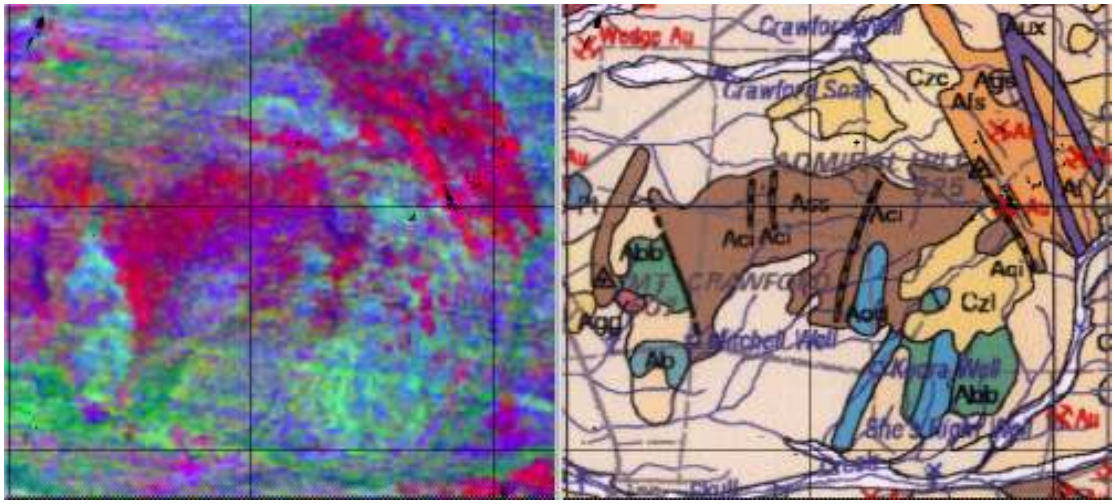

Figure 37. Zoomed in area showing (left) the decorrelation stretch of bands 13, 12 and 10 as RGB and (right) the 1:250,000 geology. The area is about 12 x 10 km.

A second close-up area is shown in Figure 38. A small area of silcrete (Czu) is mapped at A, but the image suggests that this material is far more extensive. The area of sandy colluvium associated with sandstone (Ass) is also clearly visible at B. Chert units at C, although often about 90 metres in width (D. Champion, pers. comm.) (1 pixel wide), are clearly visible. The dark tone suggests that the chert unit has a low temperature, since temperature is represented in the intensity of the decorrelation stretch (for level 1b radiance data). This is feasible for massive silica-rich materials which, having a high thermal inertia, may take a while to heat up.

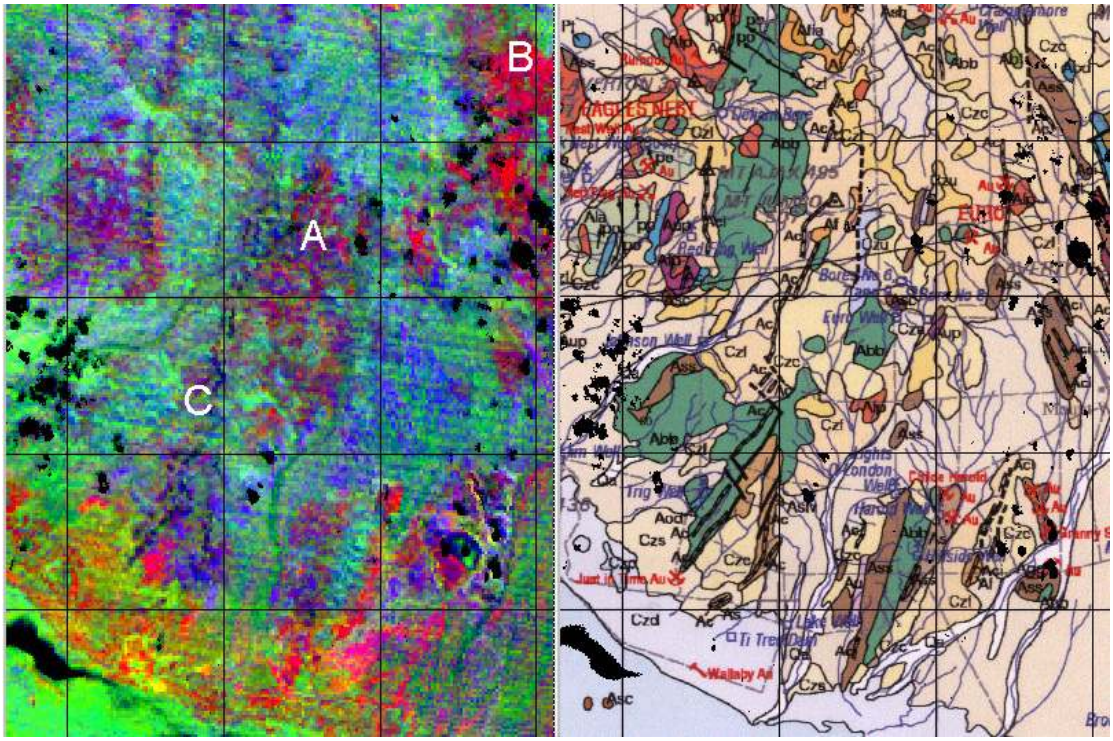

Figure 38. Zoomed-in area of the decorrelation stretch and geology showing chert and silcrete units

In this area, the silica index (b11*b11/b10/b12) (Ninomiya and Fu, 2001) is effective at mapping silica content. It removes the temperature effects discussed above and confirms the quartz content of the chert units. The basic degree index (b12/b13) does highlight basic rocks but also vegetation perhaps more strongly. The carbonate ratio (b13/b14) is extremely noisy, due to the characteristics of bands 13 and 14, but does appear to detect carbonate in drainage lines but not Czk - mapped calcrete areas.

4.0 Conclusions

In general, the ASTER data quality is good and registration between bands appears adequate for analysis. Comparisons with Landsat TM shows that ASTER has much improved spatial resolution in the VNIR and far greater spectral resolution in the SWIR.

The level 2 (AST_07) reflectance product has some significant problems both for use in visual identification of spectral features and for analysis of end-members. A gain problem in band 9 centred at 2.395 μm results in reflectance values that are much too high. Also, a strong 2.165 μm absorption feature is present in pixels with high SWIR reflectance for both the Indee and Laverton areas. It can be demonstrated for both areas that this feature is not due to minerals such as pyrophyllite, alunite or even vegetation where this feature might be expected. It is very likely that this effect is an artifact and potentially a major problem for processing since it is not present for lower SWIR reflecting materials and hence the spectral shape is corrupted by albedo effects. In this study, this problem was overcome by performing a gain and offset correction to the ASTER level 1B radiance data by subtracting scene minimum values and normalizing cloud-top signatures. After performing this correction (called RMN here), image spectral signatures were realistic and analysis for end-member abundances were more accurate, although only marginally for the Indee data.

For the Indee, Pilbara, case study area, Mixture Tuned Matched Filtering (MTMF) produced best results for mapping mineral concentrations. The areas for extraction of image end-members were defined by airborne hyperspectral HYMAP mineral maps and the accuracy of the ASTER analysis was determined by comparisons with the HYMAP data. In comparison with the airborne data, the ASTER system is prone to mixture problems and often only capable of partial separation of minerals. ASTER was effective at mapping carbonates but not the separation of dolomite and calcite. Some Fe-chlorite areas were mapped but not those areas where it is mixed with kaolinite. White mica and kaolinite abundances were effective but there was partial mixing and commission in both end-member images. Tourmaline was successful although the use of the MTMF infeasibility score was crucial to achieving good results. ASTER also achieved good results for talc (although noisy) and Fe-oxides. Interestingly, ASTER was unable to discriminate pyrophyllite, one of the most important and spectrally resolvable minerals (using hyperspectral data) possibly due to the wide bandwidth of ASTER band 5.

In the Laverton area, ASTER was not as successful at identifying individual minerals, partly due to the nature of the geology of the Eastern Goldfields Province, but also due to the lack of definitive information on ground mineral concentrations (to

enable the definition of image mineral spectral end-members). Modelling based on rock-type signatures provided useful information about rock compositions and identified units that were mapped discretely in the earlier version of the Laverton map (Gower, 1976) but not in the 2nd edition (Stewart, 2001). An amphibole end-member, identified by MNF processing was very successful (using Matched Filtering) at mapping mafic rock exposures. At one location the ASTER amphibole image identifies grossly incorrect mapping in the 2nd edition mapping that was actually correct in the 1st edition map. There is no sign of variations due to talc, serpentine or chlorite, which should mainly show up as variations in band 9. It is possible that these minerals are occurring as a relatively constant mixture detected by the amphibole end-member. It is likely that definition of these minerals could be improved if reasonably pure image end-members could be found, perhaps by the use of localized hyperspectral surveys.

Laterite mapping was also successful at Laverton and this has implications for Nickel exploration in the region. Comparison of the laterite image (analyzed with MTMF from an end-member derived from MNF processing) and the geological map (Stewart, 2001) show that the geological mapping tends to be inclusive. The image shows that laterite can be dispersed in nature and difficult to map accurately. In this way, ASTER image data can provide more accurate representation of laterites.

Even at ASTER spectral resolution, it appears that unmixing methods are necessary to produce the most accurate spatial mapping of materials. In this study, it was found that methods such as Spectral Angle Mapper (SAM) and ratios are prone to effects due to mixing, particularly those due to vegetation. The combined use of Pixel-Purity Index (PPI) and n-D visualizer is potentially effective at hunting end-members, although this method can be difficult and time-consuming and, in this study, did not provide any more information. This may be due to the spectral mixing in ASTER data at spatial and spectral scales.

The ASTER level 2 emissivity (TES) data appears to be successful at removing temperature effects from the spectral data. Compared to the VNIR-SWIR data, thermal IR (bands 10 – 14) is less useful due to the 90m spatial resolution and noise characteristics (bands 13 and 14 are very noisy). However these data were found to be valuable, particularly in the Laverton area, for mapping quartz rich units and the dispersion of associated sandy soils. Basic units are sometimes observable in the thermal data, but are often difficult to discern from vegetation, which clearly has a masking effect.

In conclusion, it is clear that ASTER represents a scientific advance on Landsat TM data. It has the clear capability of mapping multiple geological components that are often difficult to map on the ground. Given its availability at low cost, this system should be widely employed in geological studies.

5.0 References

Bierwirth, P.N., 2000. Hyperspectral Mineral Mapping and Gold Prospecting in a Low Bedrock-Exposure Terrain using HyMap in the West Pilbara, W.A.: *Proceedings*

of the 10th Australasian Remote Sensing Conference, Adelaide. [CD-ROM], Paper 56, p 814-825.

Bierwirth, P. N., Huston, D.L, and Blewett, R., 2002. Hyperspectral mapping of mineral assemblages associated with gold mineralization in the Central Pilbara, Western Australia. *Economic Geology*, Pilbara Special Issue (in press).

Boardman, J.W., Kruse, F.A., and Green, R.O. 1995. Mapping target signatures via partial unmixing of AVIRIS data. *Summaries, 5th JPL Airborne Earth Science Workshop, JPL Publication* 95-1, 1:23-26.

Ninomiya, Y., and Fu, B., 2001. Spectral Indices for Lithologic Mapping with ASTER Thermal Infrared Data Applying to a Part of Beishan Mountains, Gansu, China. Proceedings of the *IEEE 2001 International Geoscience and Remote Sensing Symposium*, Sydney.

Gillespie, A.R., Rokugawa, S., T. Matsunaga, T., Cothern, S.J., Hook, S., and Kahle, A.B., 1998. A temperature and emissivity separation algorithm for Advanced Spaceborne Thermal Emission and Reflection Radiometer (ASTER) images. *IEEE Transactions on Geoscience and Remote Sensing*, **3**6, pp. 1113-1126, 1998.

Gillespie, A. R., 1992. Enhancement of Multispectral Thermal Infrared Images: Decorrelation Contrast Stretching. *Remote Sensing of Evnvironment*, Vol 42, p 147-155.

Gower, C.F. 1976. Laverton, W.A. (1st Edition): Western Australia Geological Survey, 1:250,000 Geological Series Explanatory Notes, 30p.

Green, A. A., Berman, M., Switzer, P, and Craig, M. D., 1988, A transformation for ordering multispectral data in terms of image quality with implications for noise removal: *IEEE Transactions on Geoscience and Remote Sensing*, v. 26, no. 1, p. 65-74.

Harsanyi, J.C., and Chang, C., 1994. Hyperspectral image classification and dimensionality reduction: an orthogonal subspace projection approach. *IEEE Transactions on Geoscience and Remote Sensing*, 32, 4, pp779-784.

Hewson, R.D, Cudahy, T.J., and Huntington, J.F., 2001.Geologic and alteration mapping at Mt Fitton, South Australia, using ASTER satellite-borne data. Proceedings of the *IEEE 2001 International Geoscience and Remote Sensing Symposium*, Sydney.

Hook, S. J., Gabell, A.R., Green, A.A., and Kealy, P.S., 1992. A Comparison of Techniques for extracting emissivity information from thermal infrared data for geological studies. *Remote Sensing of Environment*, vol 42, pp123-135.

Kahle, A.B, and Alley, R. E. (1992). Separation of Temperature and Emittance in Remotely Sensed Radiance Measurements. *Remote Sensing of Environment*, 42. P107-111.

Kay, J., Handcock, R.N, Gillespie, A., Konrad, C., Burges, S., Naveh, N., and Booth, D., 2001. Stream-temperature estimation from thermal infrared images. Proceedings of the *IEEE 2001 International Geoscience and Remote Sensing Symposium*, Sydney

Kealy, P.S., and Hook, S.J., 1993. Separating Temperature and Emissivity in Thermal Infrared Multispectral Scanner Data: Implications for recovering Land Surface Temperatures. *IEEE Transactions on Geoscience and Remote Sensing*, Vol 31, No 6, pp 1155-1164.

Kruse, F. A., Lefkoff, A. B., Boardman, J. W., Heidebrecht, K. B., Shapiro, A. T., Barloon, J. P., and Goetz, A. F. H., 1993, The spectral image processing system (SIPS) - Interactive visualization and analysis of imaging spectrometer data: *Remote Sensing of Environment*, v. 44, p. 145 - 163.

Lillesand, T.M. and Kiefer, R.W., 1999. Remote Sensing and Image Interpretation, 4th Edition, Wiley and Sons, New York, 724p

[Palluconi, R., Hoover, G., Alley, R., Jentoft-Nilsen, M., and Thompson, T., 1996. An atmospheric correction method for ASTER Thermal radiometry over land, revision 2: ASTER standard data product AST09, Level 2 Radiance – TIR, land-leaving, Jet Propulsion Laboratory, Pasadena, CA, http://asterweb.jpl.nasa.gov/asterhome/atbd/ATBD-AST-04.doc.

Stewart, A.J., 2001. Laverton, W.A. (2nd Edition): Western Australia Geological Survey, 1:250,000 Geological Series Explanatory Notes, 34p.

Thorne, K., Palluconi, Takashima, and Masuda, K., 1998. Atmospheric correction of ASTER. . *IEEE Transactions on Geoscience and Remote Sensing*, Vol 36, No 4, pp 1199-1211.